

How Does El Niño Southern Oscillation Change Under Global Warming - A First Look at CMIP6

Hege-Beate Fredriksen¹, Judith Berner², Aneesh Subramanian³, and Antonietta Capotondi³

¹Department of Physics and Technology, UiT The Arctic University of Norway

²National Center for Atmospheric Research (UCAR)

³University of Colorado Boulder

November 21, 2022

Abstract

The latest generation of coupled models, the sixth Coupled Models Intercomparison Project (CMIP6), is used to study the changes in the El Niño Southern Oscillation (ENSO) in a warming climate. For the four future scenarios studied, the sea surface temperature variability increases in most CMIP6 models, but to varying degrees. This increase is linked to a weakening of the east-west temperature gradient in the tropical Pacific Ocean, which is evident across all models. Just as in previous generations of climate models, we find that many characteristics of future ENSO remain uncertain. This includes changes in dominant timescale, extra-tropical teleconnection patterns and amplitude of El Niño and La Niña events. For models with the strongest increase in future variability, the majority of the increase happens in the Eastern Pacific, where the strongest El Niño events usually occur.

1 **How Does El Niño Southern Oscillation Change Under Global Warming - A**
2 **First Look at CMIP6**

3
4 **Hege-Beate Fredriksen^{1*}, Judith Berner², Aneesh C. Subramanian³ and Antonietta**
5 **Capotondi^{4,5}**

6 ¹Department of Physics and Technology, UiT the Arctic University of Norway, Tromsø,
7 Norway.

8 ²National Center for Atmospheric Research, Boulder, CO, USA.

9 ³Atmospheric and Oceanic Sciences, University of Colorado Boulder, Boulder, CO, USA.

10 ⁴Cooperative Institute for Research in Environmental Sciences, University of Colorado, Boulder,
11 Colorado, USA.

12 ⁵NOAA Physical Sciences Laboratory, Boulder, CO, USA.

13
14 Corresponding author: Hege-Beate Fredriksen (hege-beate.fredriksen@uit.no)

15
16 **Key Points:**

- 17 • Changes in El Niño Southern Oscillations are detected for future projections in the
18 latest generation of climate models.
- 19 • Models agree on future decrease of the equatorial zonal temperature gradient, which
20 facilitates conditions for stronger El Niño events.
- 21 • El Niño and La Niña global teleconnection patterns shift in the future, but there is a
22 large uncertainty on the magnitude of the change.
- 23
24
25
26
27
28
29
30
31
32
33
34
35
36
37
38

39 **Abstract**

40 The latest generation of coupled models, the sixth Coupled Models Intercomparison Project
41 (CMIP6), is used to study the changes in the El Niño Southern Oscillation (ENSO) in a warming
42 climate. For the four future scenarios studied, the sea surface temperature variability increases in
43 most CMIP6 models, but to varying degrees. This increase is linked to a weakening of the east-
44 west temperature gradient in the tropical Pacific Ocean, which is evident across all models. Just
45 as in previous generations of climate models, we find that many characteristics of future ENSO
46 remain uncertain. This includes changes in dominant timescale, extra-tropical teleconnection
47 patterns and amplitude of El Niño and La Niña events. For models with the strongest increase in
48 future variability, the majority of the increase happens in the Eastern Pacific, where the strongest
49 El Niño events usually occur.

50

51 **Plain Language Summary**

52

53 The El Niño Southern Oscillation (ENSO) is a naturally occurring irregular oscillation in the
54 tropical Pacific Ocean alternating between warm (El Niño) and cold (La Niña) phases every 2-7
55 years. The sea surface temperature anomalies associated with ENSO are linked to variability in
56 key climate quantities, such as temperature, winds, and precipitation over many parts of the
57 globe. Hence it is of great scientific and societal interest to determine how ENSO may change in
58 a warming climate. We find that the latest generation of climate models shows changes in ENSO
59 in a warmer world. The future variability is increasing, especially in the eastern equatorial
60 Pacific, where the extreme warm events usually occur. This increase appears to be related to a
61 reduced temperature difference between the eastern and western equatorial Pacific. The global
62 weather patterns influenced by both the warm and cold events will also change, but models
63 disagree on how large these changes will be.

64

65 **1 Introduction**

66 ENSO is characterized by irregular fluctuations between cold (La Niña) and warm (El Niño)
67 conditions in the eastern and central equatorial Pacific on a timescale of 2-7 years. The warm
68 phase is associated with a weakening of the trade winds and eastward shift of convection, which
69 brings the warm waters of the west Pacific eastward. This decrease of the east-west gradient in
70 SST is concomitant with a deepening (shoaling) of the thermocline in the eastern (western)
71 equatorial Pacific. Due to its global teleconnections, ENSO is not only the dominant mode of
72 tropical interannual variability but also the leading source of forecast skill on seasonal to
73 interannual timescales in many other parts of the world (Jin et al., 2008; Barnston, 2016). It has
74 important impacts on fisheries, agriculture, hurricanes, droughts, floods, and other severe
75 weather events.

76

77 A rich body of work has studied the response of ENSO to global warming in previous
78 generations of climate models, but there has been no clear consensus on how ENSO will change
79 under global warming (e.g., Collins et al. 2010, Yeh et al. 2012, Guilyardi et al. 2012, Stevenson
80 2012, Taschetto et al. 2014, Cai et al. 2015a, Berner et al. 2020). The CMIP6 archive provides a
81 new opportunity to study the ENSO response to prescribed radiative forcing (Eyring et al., 2016)
82 across a number of state-of-the-art climate models. Here, we will focus on the question: “**To**

83 **which degree do CMIP6 models agree on ENSO changes in different global warming**
84 **scenarios?”.**

85

86 Assessments of ENSO future changes must account for the diversity of ENSO spatial patterns
87 (Ashok et al., 2007; Capotondi et al., 2015). ENSO events display a broad spectrum of anomaly
88 centers ranging from the dateline (CP events) to the far eastern equatorial Pacific (EP events,
89 Capotondi et al., 2015; Capotondi et al., 2020), and the exact location of the warming centers
90 may be model dependent (Cai et al., 2018). This diversity can have very important consequences
91 for atmospheric teleconnections and worldwide impacts (Ashok et al., 2007; Larkin and
92 Harrison, 2005; Patricola et al., 2018), and needs to be considered when examining ENSO
93 response to global warming.

94

95 Several studies have shown that ENSO characteristics, such as period and growth rate are highly
96 dependent on the tropical Pacific mean state (Battisti and Hirst, 1989; Fedorov and Philander,
97 2001). In particular, the mean temperature in the eastern equatorial Pacific, which controls the
98 temperature gradient between the West Pacific warm pool and Eastern Pacific cold tongue, as
99 well as the zonal slope of the equatorial thermocline, are important factors controlling ENSO's
100 stability characteristics and ENSO diversity (Fedorov and Philander, 2000, 2001; Capotondi and
101 Sardeshmukh, 2015). Specifically, a deeper thermocline in the eastern equatorial Pacific,
102 accompanied by reduced easterly winds and weaker zonal SST gradient, favors longer periods
103 and larger SST anomalies in the eastern equatorial Pacific, as observed, for instance, in the 1980s
104 and 1990s (Fedorov and Philander, 2001, Capotondi and Sardeshmukh, 2017) relative to
105 previous decades. Another controlling factor is cross-equatorial winds, which can significantly
106 influence ENSO properties but with larger uncertainties in future scenarios (Hu and Fedorov,
107 2018). The ENSO mean state relationship is further complicated by the presence of ENSO
108 asymmetries, with warm events typically stronger than cold events in the eastern Pacific
109 (positive skewness), and cold anomalies somewhat larger than warm anomalies in the central
110 Pacific (negative skewness), an aspect of ENSO that may be indicative of system nonlinearities.
111 Such nonlinearities may, in turn, lead to a “rectification” of ENSO variations into the mean state,
112 resulting in a low-frequency modulation of equatorial SSTs that are El Niño-like. Indeed,
113 Karamperidou et al. (2017) find a significant relationship between ENSO amplitude changes and
114 the correlation between the patterns of ENSO and SST trends.

115

116 Analyses of previous generations of climate models reported a weakening of the zonal SST
117 gradient, and of the atmospheric Walker circulation across the majority of the models, a
118 consensus that did not translate, however, in a consistent change in ENSO amplitude, as
119 measured by commonly used ENSO indices (e.g., the Niño3.4 index) that are averages of SST
120 anomalies at a fixed location. Given the differences in ENSO spatial patterns across models, a
121 better model agreement was found, albeit for a selected group of models, when indices that
122 accounted for the ENSO patterns unique to each model were used (Cai et al., 2018 Carréric et al.,
123 2019). The selection criterion was based on a metric of model nonlinearity, as encapsulated by
124 the coefficient α of the nonlinear relationship between the two leading Principal Components
125 (PCs) of SST in the equatorial Pacific (Karamperidou et al., 2017). Models in the CMIP5 archive
126 with a parameter α in the pre-industrial control simulations close to the observed value (-0.29)
127 appeared to have a balance of (linear) ENSO feedbacks in better agreement with observations
128 and exhibited a warming trend in the eastern equatorial Pacific (Karamperidou et al., 2017). The

129 parameter α also appeared to be associated with values of SST skewness in the eastern and
130 central equatorial Pacific similar to the observed values, as well as a “realistic” separation of EP
131 and CP ENSO events (Cai et al., 2018). An increase in ENSO amplitude was found by Cai et al.
132 (2018) in those models with values of α relatively close to the observed in the historical model
133 simulations. This increase in amplitude was attributed to both the enhanced mean warming and
134 increased vertical stratification in the eastern equatorial Pacific. In this study, we revisit the
135 relationship between changes in ENSO amplitude and mean state changes in the latest generation
136 of climate models with a primary focus on the connection between changes in ENSO amplitude
137 and changes in the mean zonal SST gradient.

138
139 A rather robust response detected in previous generations of climate models is the projected
140 poleward shift of the jet stream (Yin 2005), which changes the atmospheric meridional gradients,
141 and thus affects tropical-extratropical teleconnection patterns (Stevenson 2012; Stevenson et al.
142 2012). Hence, extra-tropical teleconnection patterns may change under climate change scenarios,
143 even if ENSO itself does not change significantly. This aspect is also examined in our analysis of
144 the CMIP6 models.

145
146 To assess the degree of agreement among the CMIP6 models on the ENSO change under
147 different warming scenarios, we use a number of established diagnostics. First, we investigate
148 changes in power spectral densities, total variance, and zonal SST gradient. Then we examine
149 variance changes in the context of ENSO diversity, and at last, we investigate global sea-level
150 pressure teleconnection patterns during future El Niño and La Niña events.

151 **2 Data and methods**

152 Our analysis focuses on the projected change under four different Shared Socioeconomic
153 Pathways (SSP) (O'Neill et al. 2016). The four SSP scenarios are expected to have an
154 approximate forcing of 2.6, 4.5, 7.0 and 8.5 W/m² in the year 2100, as denoted by the last two
155 digits of the names of the scenarios. Results obtained for these four future scenarios (covering the
156 86-yr period 2015-2100) are compared to those from the control simulation (piControl). Since
157 different models have a different number of ensemble members, for a fair comparison we use
158 only one member for each future scenario.

159
160 However, due to a large level of internal variability, one ensemble member may be insufficient
161 to robustly detect inter-scenario differences in variance. Hence we focus only on the significant
162 changes in each scenario relative to the pre-industrial control. Establishing significant variance
163 changes between scenarios, or between scenarios and the historical period requires several
164 ensemble members, e.g. like the 33-member ensemble of CESM1 used by Berner et al. (2020).

165
166 The analyses are performed for eleven models having a control simulation with at least 499
167 years. For all piControl simulations longer than 500 years, we only study the first 500 years.
168 Changes from the piControl are analyzed to focus on the models' response to anthropogenic
169 forcing rather than evaluating model skill over the historical period. The confidence intervals of
170 the piControl simulations used for analyses in Figures 1, 2, and 3 are computed by first splitting
171 the 500 yr records into 86 yr segments with 56 yr overlap. For each segment, we compute the
172 quantity of interest in the same way as we would for the future scenarios, and determine the

173 range of possible values across segments. Changes from the piControl are considered statistically
174 significant if they are outside this range.

175

176 Details regarding the detrending method, spectral analysis, definition of ENSO diversity, and
177 ENSO teleconnections diagnostics are provided in Supplementary Text S1.

178 **3 Results**

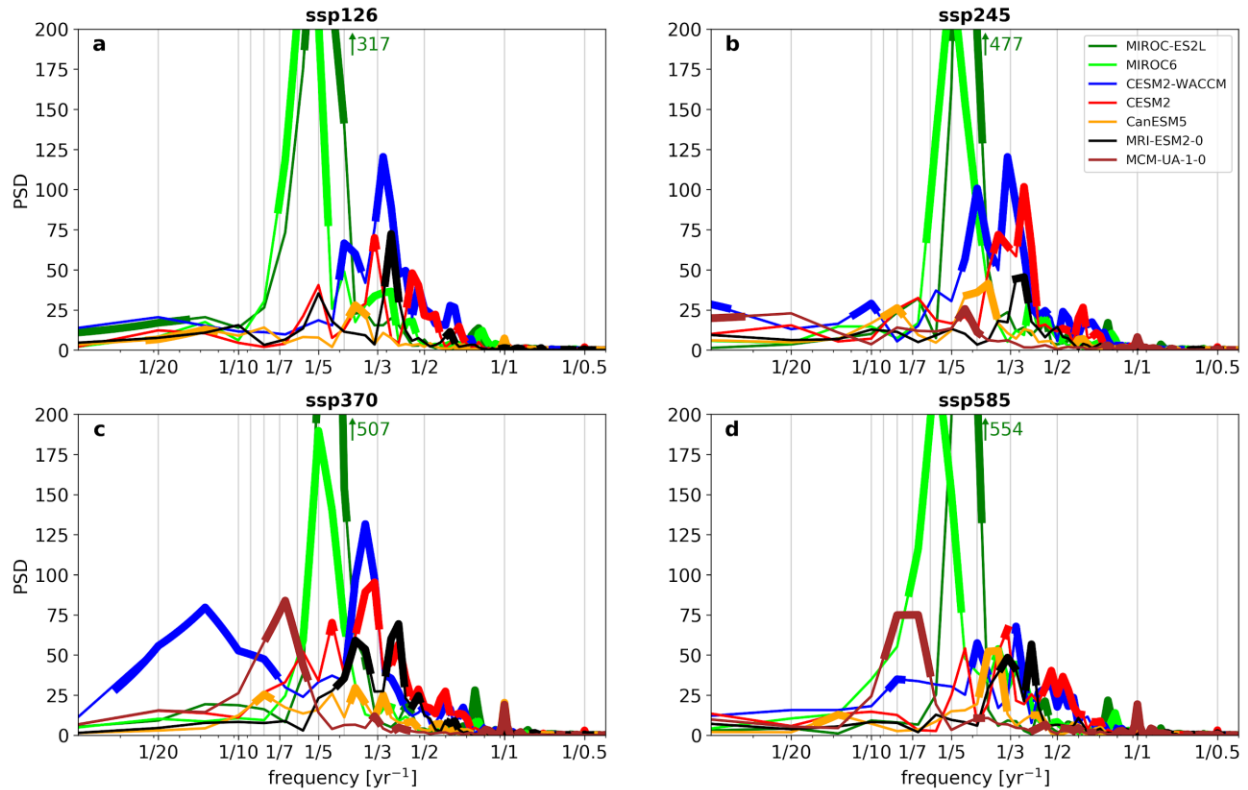
179 3.1 Power Spectral Density of Niño 3.4-index

180

181 The Niño 3.4-index, defined as the area average of monthly SST anomalies in the region 5°S-
182 5°N, 170°W-120°W, is a commonly used index to describe variability associated with ENSO
183 (see Supplementary Text S1 for details on method). The power spectra of the Niño 3.4-index
184 obtained from detrended scenarios show a wide range of variability with spectral peaks in the 2-7
185 year range (Fig.1 and Supplementary Fig.1), demonstrating the CMIP6 models' ability to
186 produce a quasi-oscillatory behavior that is reminiscent of ENSO in nature.

187

188 Figure 1 shows the seven models with the most marked changes in the spectra of future
189 scenarios. The most significant increases in variability are for the models MIROC6 and MIROC-
190 ES2L. MIROC-ES2L is the model with the most regular periodic variations, centered at periods
191 of about 5 years (Supplementary Fig.1). CESM2-WACCM and CESM2 also show significant
192 increases in power for most future scenarios with CESM2-WACCM showing the largest increase
193 around 3 years and CESM2 showing an increase at 1.5-3 year periodicities. CanESM5 shows a
194 small increase in power, mainly at the seasonal cycle and at periods of 3-4 years. The limited
195 duration of the scenario simulations (86 years) makes it difficult to estimate subtleties in the
196 future change of spectra. In particular, it is hard to assess whether the increase in power is
197 proportional to the radiative forcing.



198
 199 **Figure 1:** Power spectral density (PSD) of the detrended monthly Niño 3.4-indices for scenarios
 200 a) ssp126, b) ssp245, c) ssp370, d) ssp585 for CMIP6 models. PSDs that are statistically
 201 significantly different from pre-industrial internal variability (shown only in Supplementary Fig.
 202 S1) are shown with a thick line. The green numbers denote the maximum power for the model
 203 MIROC-ES2L.

204

205

206

207

3.2 Changes in Variance of Niño 3.4-index and zonal temperature gradient

208

209

210

211

212

213

214

215

216

217

218

219

220

221

222

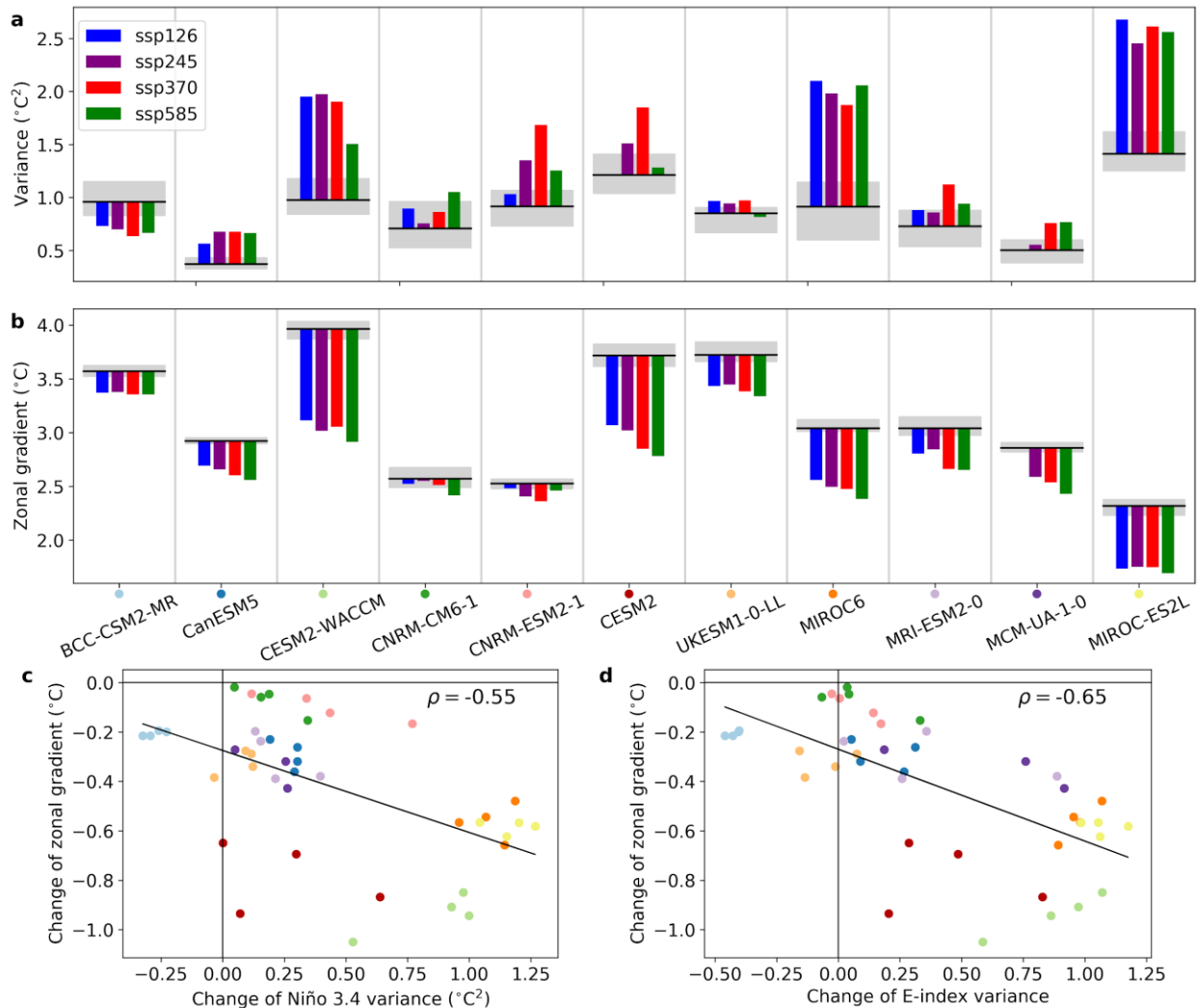
223

Another important metric to assess ENSO changes is the variance of the Niño 3.4-index. All but one model show a significant increase in variance for most scenarios (Fig. 2a), but we observe no correlation between the magnitude of forcing and variance change. As the change in mean SST in the Niño3.4-region is proportional to the forcing (Supplementary Fig. S2), we conclude that there is no obvious relation between changes in variance and mean SST either.

The strength of ENSO variability has been linked to the east-west SST gradient in the Tropical Pacific. As this gradient weakens, westerly wind anomalies can more readily extend eastward and initiate strong warm events (Xie et al., 2018). Strikingly, all models agree that the east-west SST gradient weakens in future scenarios. Furthermore, in most models this weakening is proportional to the magnitude of the radiative forcing. This suggests an anti-correlation between the change in gradient and change in SST variance. Ten out of the eleven CMIP6 models show a decrease in SST gradient concurrent with an increase in SST variance (Fig. 2c) with a statistically significant ($p\text{-value} = 1.52 \cdot 10^{-4}$) correlation of -0.55 . We expect that some of the scatter in Fig. 2c is due to the large internal ENSO variability (Berner et al., 2020) and the

224 uncertainty in the functional relationship displayed in Fig. 2c might be reduced if models with
 225 several ensemble members were analyzed.

226
 227



228
 229 **Figure 2:** a) Variance of temperature anomalies in the Niño 3.4 region [$5^{\circ}\text{S} - 5^{\circ}\text{N}$, $170^{\circ}\text{W} -$
 230 120°W] for each model and scenario after detrending and removing the seasonal cycle (see
 231 Supplementary Text S1), shown as differences from the piControl estimate using the first 500
 232 years (black line). b) The black lines show the piControl mean of the east-west temperature
 233 gradient, and the colored bars the mean change from piControl over the 86-year period 2015-
 234 2100 in the future scenarios. Temperatures in the west are averaged over the region $5^{\circ}\text{S} - 5^{\circ}\text{N}$,
 235 $120^{\circ}\text{E} - 170^{\circ}\text{E}$, and in the east over the Niño3 region [$5^{\circ}\text{S} - 5^{\circ}\text{N}$, $150^{\circ}\text{W} - 90^{\circ}\text{W}$]. Positive
 236 values mean the west is warmer than the east. In both panels, the light gray shading denotes the
 237 spread of these quantities in 86-year overlapping segments from the first 500 years of piControl,
 238 ranging from the minimum to the maximum estimates. c) Scatterplot and correlation coefficient
 239 of data in a) and b). d) As in c), but with E-index variance from the next section along x-axis.

240
 241
 242

3.3 ENSO diversity

243 A single index, like the Niño 3.4-index, is insufficient to capture the full range of ENSO
244 expressions and the temporal evolution of ENSO events. In particular, more than one index is
245 needed to describe differences in ENSO spatial patterns. Several indices have been proposed to
246 describe this diversity in El Niño spatial patterns (Capotondi et al., 2020). Here we use the
247 approach introduced by Takahashi et al. (2011) to construct the E- and C-indices, which describe
248 events with enhanced variability in the eastern and central Pacific, respectively (see
249 Supplementary Text S1, and Supplementary Fig. S3 for examples of their associated patterns).
250 These indices are computed as linear combinations of the two leading Principal Components
251 (PCs) of SST anomalies in the equatorial Pacific, and thus describe the patterns of variability
252 typical of each model.

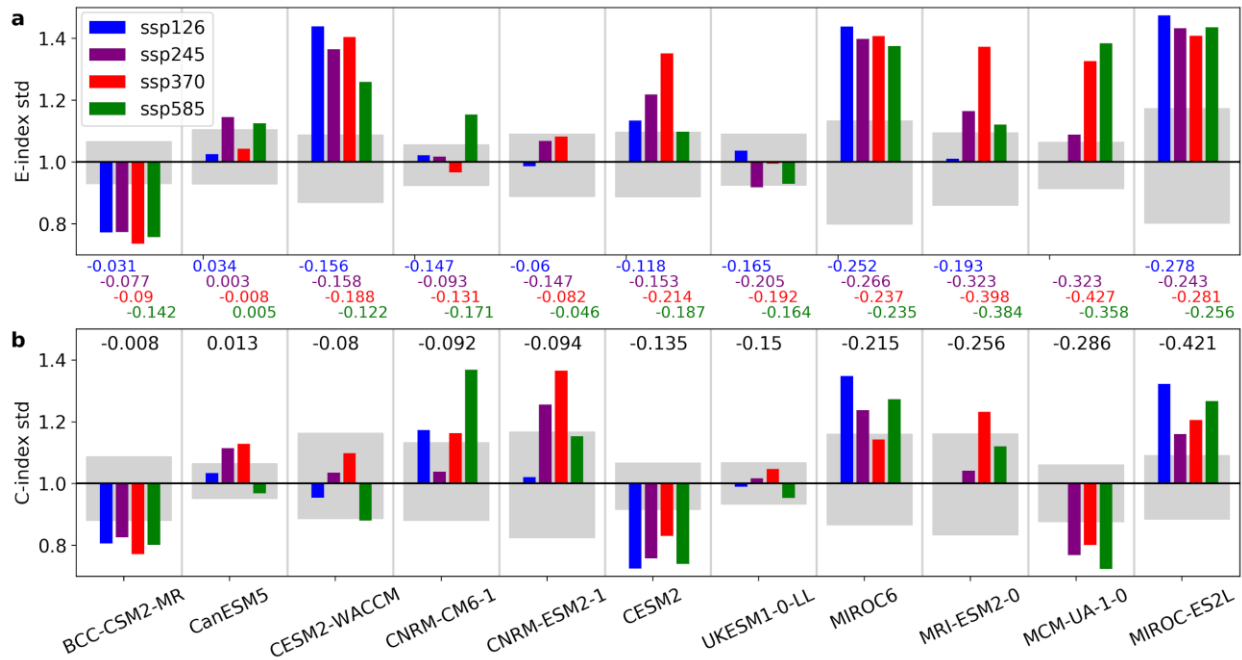
253
254 Fig. 3a shows the standard deviation of the E-index in the four climate change scenario
255 simulations relative to the control simulation, whose standard deviation was normalized to one.
256 Instead of arbitrarily selecting the models by their α value in the control simulation, we include
257 all the models, and order them by increasing magnitude of α , to highlight the impact of this
258 parameter on the changes in ENSO variance. While the only model showing a significant
259 decrease in ENSO variance is the model with the smallest absolute value of α , no clear
260 relationship can be seen in Fig. 3a between the variance changes and the magnitude of α . In
261 addition, the parameter α may change in the scenario simulations relative to the control
262 simulations (see Supplementary Figure S5, where the nonlinear fit of PC1 and PC2 is shown for
263 all models and simulations), and is not an intrinsic property of each model, as implied in the
264 studies of Karamperidou et al. (2017) and Cai et al. (2018).

265
266 When the change of the variance in the E-index is plotted against the change of the east-west
267 SST gradient, we see an even stronger relationship between the two quantities, as quantified by a
268 correlation coefficient of -0.65 with p-value = $1.97 \cdot 10^{-6}$ (Fig 2d): generally, a weakening of the
269 SST gradient will lead to an increase in the variance of Eastern Pacific (EP) events.

270
271 Previous studies (Stevenson et al., 2012; Bellenger et al., 2014; Cai et al. 2015b; Capotondi
272 2015) have also suggested an increase in the frequency of extreme La Niña events with global
273 warming due to a strengthened zonal temperature gradient between the Maritime Continent and
274 the central Pacific, where La Niña events typically peak. This should be reflected in the standard
275 deviation of the C-index (Fig. 3b). Robust increases in the C-index standard deviation are seen in
276 some models, but in some cases the standard deviations show a significant decrease (BCC-
277 CSM2-MR, CESM2, MCM-US-1-0) or insignificant changes (CanESM5, CESM2-WACCM,
278 UKESM1-0-LL), indicating a larger degree of uncertainty in the projected changes of La Niña's
279 (as well as CP El Niño) amplitude relative to the EP El Niño events.

280

281



282

283 **Figure 3:** The standard deviations of the E-index (a) and C-index (b), shown as deviations from
 284 the piControl value. piControl standard deviation is by definition 1, due to normalization. The
 285 shaded gray areas show the spread of standard deviations in piControl segments of equal lengths
 286 as the future scenarios, ranging from the minimum to the maximum value. The black numbers
 287 are piControl α 's, whose magnitude is increasing from left to right. The colored numbers are the
 288 α values for future scenarios.

289

290

3.4 ENSO teleconnections

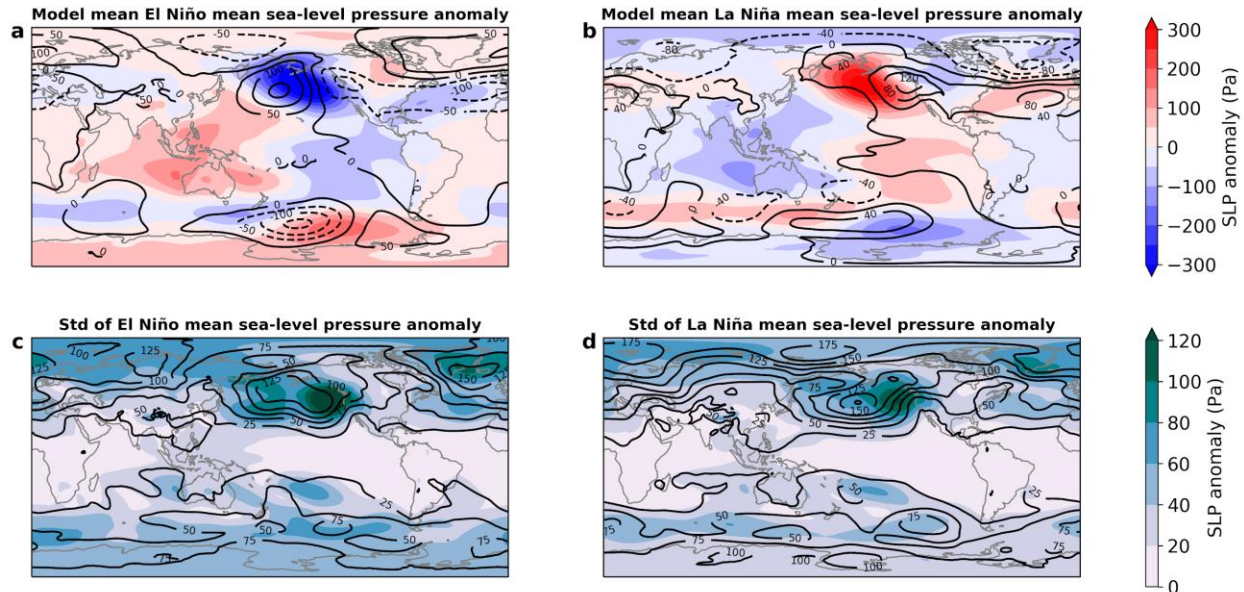
291

292 ENSO, primarily a tropical ocean-atmosphere coupled process, has an influence globally via
 293 atmospheric and oceanic teleconnections (Alexander et al., 2002; Deser et al., 2012; Yeh et al.
 294 2018). The teleconnection diagnostics used in this study follows that of Stevenson et al. (2012).
 295 El Niño and La Niña composites for the ensemble mean of CMIP6 are computed for sea-level
 296 pressure (SLP) anomalies. The mean SLP anomalies of the ensemble mean show the canonical
 297 features of the Aleutian low deepening during warm events and anomalous higher pressures
 298 during cold events with pressures of opposite sign in the Southern Hemisphere at the same
 299 longitude. Teleconnection changes are then evaluated by comparing the ssp585 and piControl.
 300 The changes in the future climate across the CMIP6 ensemble are shown in the black contours in
 301 Fig. 4. Marked changes in the Aleutian island region and the southern ocean region are observed.
 302 The atmospheric teleconnections show a weakening signal in the ssp585 scenario compared to
 303 the piControl. This has been studied in previous versions of similar climate models and partly
 304 been attributed to the increase in atmospheric static stability in warmer climates (Ma et al., 2012;
 305 Stevenson et al., 2012)

306

307 The spatial patterns of the teleconnection of warm events in the future scenario shifts poleward
 308 and eastward in the CMIP6 ensemble mean over the Aleutian island regions and the Southern
 309 Ocean regions. The eastward shift can be seen as a weakening of the pressure anomalies in the

310 west, and a strengthening in the east in Figure 4a. This has also been seen in the model versions
 311 from CMIP5 and CMIP3 (Meehl and Teng 2007; Stevenson et al., 2012). The teleconnection
 312 patterns for La Niña events show a zonal elongation over the Aleutian region instead of a spatial
 313 shift, and a general weakening of the Southern Ocean anomalies as seen in Figure 4b. The
 314 standard deviation across the ensemble members is shown in Figure 4 c,d, where the largest
 315 variance is observed over the Aleutian region, which is also the region of the strongest
 316 teleconnection from the Tropical Pacific. This ensemble spread indicates the uncertainty in the
 317 observed changes to the ENSO teleconnections due to internal variability and differences in
 318 model physics.
 319



320
 321 **Figure 4:** DJF ENSO teleconnection pattern shown as mean SLP anomalies across models for
 322 piControl (colors) for a) El Niño and b) La Niña, and the corresponding changes of mean SLP
 323 anomalies for future scenario ssp585 (black contours). c) El Niño and d) La Niña model spread
 324 of the piControl SLP anomalies (colors) and change for future scenario ssp585 (black contours),
 325 measured by the standard deviation.
 326

327

328

4 Summary and Conclusion

329

330 In this study, we have provided a first look at the projected change of ENSO in four CMIP6
 331 future scenarios. Our analysis focused on understanding to which degree the various models
 332 agree about projected changes. As reported for the previous intercomparison projects CMIP3 and
 333 CMIP5, ENSO is characterized by a high degree of variability and diversity (e.g., Collins et al.
 334 2010, Yeh et al. 2012, Guilyardi et al. 2012, Taschetto et al. 2014) across models and long data
 335 records are needed to establish statistically significant changes in its characteristics. While there
 336 continues to be no across-model consensus on the change in variance and spectra of ENSO, we
 337 see agreement on some emerging signals:
 338

339

- 1) In all eleven models the east-west gradient of SST decreases in the future, with larger
 340 decreases in the scenarios with higher radiative forcing. A weaker gradient has been

341 associated with increased likelihood of strong East Pacific warm events, which have
342 large socio-economic impacts.

343

344 2) Out of the eleven models ten show a significant increase in variance of SST in the
345 Niño 3.4 region for at least one SSP and four models for all future scenarios. This
346 increase in variance is likely linked to the decrease in the zonal temperature gradient
347 and increase of strong warm events.

348

349 3) While all CMIP6 models are able to produce quasi-oscillatory behavior reminiscent
350 of ENSO, there is a wide range of variability with spectral peaks in the 2-7 year
351 range. Seven out of the eleven CMIP6 models show a significant increase in power
352 spectral density in the ENSO band with periods ranging from 3-7 years.

353

354 4) In eight out of the eleven models we see a significant increase in the standard
355 deviation of the E-index for at least one SSP. Previous studies (Cai et al. 2015a, 2018)
356 have linked the change in variability of the E-index to model's nonlinearities, a
357 relationship that does not seem to be as robust for the models studied here.

358

359 5) In nine of the eleven models, the centers of the extra-tropical teleconnection pattern
360 shift eastward and poleward for warm events. However, since the centers of the
361 teleconnections coincide with the regions of largest internal variability, it is hard to
362 establish significance for this shift.

363

364 The eleven CMIP6 models analyzed here appear to be in better agreement than the models
365 contributing to the previous intercomparison projects CMIP3 and CMIP5. However, their
366 projections still differ in many key aspects of ENSO, such as the spectra, the representation of
367 ENSO diversity and the change in extra-tropical teleconnection patterns.

368 No attempt has been made here to evaluate the models' skill in representing observed ENSO
369 variability. A careful assessment of the models' fidelity in representing ENSO during the
370 historical period together with in-depth process-level analysis might enable to further constrain
371 the projected change in ENSO in current and future CMIP simulations.

372

373 **Acknowledgements**

374 This work was started at the NCAR CMIP6 Hackathon, Boulder, Oct 16-18, 2019. We would
375 like to thank its organizers and sponsors. H.-B.F. would like to thank Dr. Peter Lauritzen and the
376 Atmospheric Modeling and Prediction (AMP) Section at NCAR for hosting her in the fall of
377 2019. NCAR is sponsored by the National Science Foundation. ACS would like to acknowledge
378 support from NOAA CVP grant number NA18OAR4310405. AC acknowledges support from
379 the NOAA Climate Program Office Climate Variability and Predictability program.

380

381 **Author contributions**

382 All authors contributed to designing the study, interpreting results, and writing the paper. H.-B.
383 F. performed all the analyses.

384

385 **Data availability**

386 The CMIP6 data are available through <https://esgf-node.llnl.gov/search/cmip6/>.

387

388 **Code availability**389 Code used for this paper will be available in Github: https://github.com/Hegebf/enso_paper

390

391 **References**

392 Alexander, M. A., Bladé, I., Newman, M., Lanzante, J. R., Lau, N., & Scott, J. D. (2002), The
393 atmospheric bridge: The influence of ENSO teleconnections on air–sea interaction over the
394 global oceans. *Journal of Climate*, 15, 2205–2231. [https://doi.org/10.1175/1520-](https://doi.org/10.1175/1520-0442(2002)015<2205:TABTIO>2.0.CO;2)
395 0442(2002)015<2205:TABTIO>2.0.CO;2

396

397 Ashok, K., Behera, S. K., Rao, S. A., Weng, H., & Yamagata, T. (2007), El Niño Modoki and its
398 possible teleconnection, *Journal of Geophysical Research*, 112, C11007.

399 <https://doi.org/10.1029/2006JC003798>

400

401 Barnston, A.G. (2016), Evolution of ENSO Prediction over the Past 40 Years. *Climate*
402 *Prediction S&T Digest*, 94-101.

403

404 Battisti, D. S., & Hirst, A. C. (1989), Interannual Variability in a Tropical Atmosphere-Ocean
405 Model: Influence of the Basic State, Ocean Geometry and Nonlinearity. *Journal of the*
406 *Atmospheric Sciences*, 46 (12), 1687-1712.

407 [https://doi.org/10.1175/1520-0469\(1989\)046<1687:IVIATA>2.0.CO;2](https://doi.org/10.1175/1520-0469(1989)046<1687:IVIATA>2.0.CO;2)

408

409 Bellenger, H., Guilyardi, É., Leloup, J., Lengaigne, M., & Vialard, J. (2014), ENSO
410 representation in climate models: from CMIP3 to CMIP5. *Climate Dynamics*, 42, 1999-2018.

411 <https://doi.org/10.1007/s00382-013-1783-z>

412

413 Berner, J., Christensen, H. M., & Sardeshmukh, P. D. (2020), Does ENSO regularity increase in
414 a warming climate? *Journal of Climate*, 33, 1247-1259. [https://doi.org/10.1175/JCLI-D-19-](https://doi.org/10.1175/JCLI-D-19-0545.1)

415 0545.1

416

417 Cai, W., Santoso, A., Wang, G., Yeh, S.-W., An, S., & Cobb, K. M. et al. (2015a), ENSO and
418 greenhouse warming. *Nature Climate Change*, 5, 849-859. <https://doi.org/10.1038/nclimate2743>

419

420 Cai, W., Wang, G., Santoso, A., McPhaden, M. J., Wu, L., & Jin, F.-F. et al. (2015b), Increased
421 frequency of extreme La Niña events under greenhouse warming. *Nature Climate Change*, 5,

422 132-137. <https://doi.org/10.1038/nclimate2492>

423

424 Cai, W., Wang, G., Dewitte, B., Wu, L., Santoso, A., & Takahashi, K. et al. (2018), Increased
425 variability of eastern Pacific El Niño under greenhouse warming. *Nature*, 564, 201-206.

426 <https://doi.org/10.1038/s41586-018-0776-9>

427

428 Capotondi, A. (2015), Extreme La Niña events to increase. *Nature Climate Change*, 5, 100-101.

429 <https://doi.org/10.1038/nclimate2509>

430

431 Capotondi, A., & Sardeshmukh, P. D. (2015), Optimal precursors of different types of ENSO
432 events. *Geophysical Research Letters*, 42, 9952-9960. <https://doi.org/10.1002/2015GL066171>

- 433
434 Capotondi, A., & Sardeshmukh, P. D. (2017), Is El Niño really changing? *Geophysical Research*
435 *Letters*, 44, 8548-8556. <https://doi.org/10.1002/2017GL074515>
436
- 437 Capotondi, A., Wittenberg, A. T., Newman, M., Di Lorenzo, E., Yu, J., & Braconnot, P. et al.
438 (2015), Understanding ENSO diversity. *Bulletin of the American Meteorological Society*, 96,
439 921-938. <https://doi.org/10.1175/BAMS-D-13-00117.1>
440
- 441 Capotondi, A., Wittenberg, A. T., Kug, J.-S., Takahashi, K., & McPhaden, M. (2020), ENSO
442 Diversity. AGU Monograph on “El Niño Southern Oscillation in a changing climate”, A.
443 Santoso, W. Cai, and M. McPhaden, Editors, accepted.
444
- 445 Carréric, A., Dewitte, B., Cai, W., Capotondi, A., Takahashi, K., & Yeh, S.-W. et al. (2019),
446 Change in strong Eastern Pacific El Niño events dynamics in the warming climate. *Climate*
447 *Dynamics*, 54, 901-918. <https://doi.org/10.1007/s00382-019-05036-0>
448
- 449 Collins, M., An, S., Cai, W., Ganachaud, A., Guilyardi, E., & Jin, F.-F. et al. (2010), The impact
450 of global warming on the tropical Pacific Ocean and El Niño. *Nature Geoscience*, 3, 391-397.
451 <https://doi.org/10.1038/ngeo868>
452
- 453 Deser, C., Phillips, A. S., Tomas, R. A., Okumura, Y. M., Alexander, M. A., & Capotondi, A. et
454 al. (2012), ENSO and Pacific Decadal Variability in the Community Climate System Model
455 Version 4. *Journal of Climate*, 25, 2622-2651. <https://doi.org/10.1175/JCLI-D-11-00301.1>
- 456 Eyring, V., Bony, S., Meehl, G. A., Senior, C. A., Stevens, B., & Stouffer, R. J. et al. (2016),
457 Overview of the Coupled Model Intercomparison Project Phase 6 (CMIP6) experimental design
458 and organization. *Geoscientific Model Development*, 9(5), 1937-1958.
459 <https://doi.org/10.5194/gmd-9-1937-2016>
- 460 Fedorov, A. V., & Philander, S. G. (2000), Is El Niño Changing? *Science*, 288, 1997-2002.
461 <https://doi.org/10.1126/science.288.5473.1997>
- 462 Fedorov, A. V., & Philander, S. G. (2001), A Stability Analysis of Tropical Ocean-Atmosphere
463 Interactions: Bridging Measurements and Theory for El Niño. *Journal of Climate*, 14, 3086-
464 3101, [https://doi.org/10.1175/1520-0442\(2001\)014<3086:ASAOTO>2.0.CO;2](https://doi.org/10.1175/1520-0442(2001)014<3086:ASAOTO>2.0.CO;2)
- 465 Guilyardi, E., Bellenger, H., Collins, M., Ferrett, S., Cai, W., & Wittenberg, A. (2012), A first
466 look at ENSO in CMIP5. *Clivar Exchanges* 17(58), 29-32.
467
- 468 Hu, S., & Fedorov, A. V. (2018), Cross-equatorial winds control El Niño diversity and change.
469 *Nature Climate Change*, 8, 798-802. <https://doi.org/10.1038/s41558-018-0248-0>
470
- 471 Jin, E. K., Kinter, J. L., Wang, B., Park, C.-K., Kang, I.-S., & Kirtman, B. P. et al. (2008),
472 Current status of ENSO prediction skill in coupled ocean-atmosphere models. *Climate*
473 *Dynamics*, 31, 647-664. <https://doi.org/10.1007/s00382-008-0397-3>

- 474
475 Karamperidou, C., Jin, F.-F., & Conroy, J. L. (2017), The importance of ENSO nonlinearities in
476 tropical pacific response to external forcing. *Climate Dynamics*, 49, 2695-2704.
477 <https://doi.org/10.1007/s00382-016-3475-y>
478
- 479 Larkin, N. K., & Harrison, D. E. (2005), Global seasonal temperature and precipitation
480 anomalies during El Niño autumn and winter. *Geophysical Research Letters*, 32, L16705.
481 <https://doi.org/10.1029/2005GL022860>
482
- 483 Ma, J., Xie, S., & Kosaka, Y. (2012), Mechanisms for tropical tropospheric circulation change in
484 response to global warming. *Journal of Climate*, 25, 2979–2994. [https://doi.org/10.1175/JCLI-D-](https://doi.org/10.1175/JCLI-D-11-00048.1)
485 [11-00048.1](https://doi.org/10.1175/JCLI-D-11-00048.1)
486
- 487 Meehl, G. A., & Teng, H. (2007), Multi-model changes in El Niño teleconnections over North
488 America in a future warmer climate. *Climate Dynamics*, 29, 779–790.
489 <https://doi.org/10.1007/s00382-007-0268-3>
490
- 491 O'Neill, B. C., Tebaldi, C., van Vuuren, D. P., Eyring, V., Friedlingstein, P., & Hurtt, G. et al.
492 (2016), The scenario model intercomparison project (ScenarioMIP) for CMIP6. *Geoscientific*
493 *Model Development*. 9, 3461-3482. <https://doi.org/10.5194/gmd-9-3461-2016>
494
- 495 Patricola, C. M., Camargo, S. J., Klotzbach, P. J., Saravanan, R., & Chang, P. (2018), The
496 influence of ENSO flavors on western North Pacific tropical cyclone activity. *Journal of*
497 *Climate*, 31, 5395-5416. <https://doi.org/10.1175/JCLI-D-17-0678.1>
498
- 499 Stevenson, S., Fox-Kemper, B., Jochum, M., Neale, R., Deser, C., & Meehl, G. (2012), Will
500 there be a significant change to El Niño in the 21st century? *Journal of Climate*, 25, 2129–2145.
501 <https://doi.org/10.1175/JCLI-D-11-00252.1>
502
- 503 Stevenson, S. L. (2012), Significant changes to ENSO strength and impacts in the twenty-first
504 century: Results from CMIP5. *Geophysical Research Letters*, 39, L17703.
505 <https://doi.org/10.1029/2012GL052759>
506
- 507 Taschetto, A. S. Gupta, A. S., Jourdain, N. C., Santoso, A., Ummenhofer, C. C., & England, M.
508 H. (2014), Cold tongue and warm pool ENSO events in CMIP5: mean state and future
509 projections. *Journal of Climate*, 27, 2861-2885. <https://doi.org/10.1175/JCLI-D-13-00437>
510
- 511 Takahashi, K., Montecinos, A., Goubanova, K., & Dewitte, B. (2011), ENSO regimes:
512 Reinterpreting the canonical and Modoki El Niño. *Geophysical Research Letters*, 38, L10704.
513 <https://doi.org/10.1029/2011GL047364>
514
- 515 Xie, S.-P., Peng, Q., Kamae, Y., Zheng, X. T., Tokinaga, H., & Wang, D. (2018), Eastern Pacific
516 ITCZ dipole and ENSO diversity. *Journal of Climate*, 31, 4449-4462.
517 <https://doi.org/10.1175/JCLI-D-17-0905.1>
518

519 Yeh, S.-W., Ham, Y. G., & Lee, J. Y. (2012), Changes in the tropical Pacific SST trend from
520 CMIP3 to CMIP5 and its implication of ENSO. *Journal of Climate*, 25, 7764-7771.
521 <https://doi.org/JCLI-D-12-00304.1>

522
523 Yeh, S.-W., Cai, W., Min, S.-K., McPhaden, M. J., Dommenges, D., & Dewitte, B. et al. (2018),
524 ENSO atmospheric teleconnections and their response to greenhouse gas forcing. *Reviews of*
525 *Geophysics*, 56, 185-206. <https://doi.org/10.1002/2017RG000568>

526
527 Yin, J. H. (2005), A consistent poleward shift of the storm tracks in simulations of 21st century
528 climate. *Geophysical Research Letters*, 32, L18701. <https://doi.org/10.1029/2005GL023684>

529
530

Figure 1.

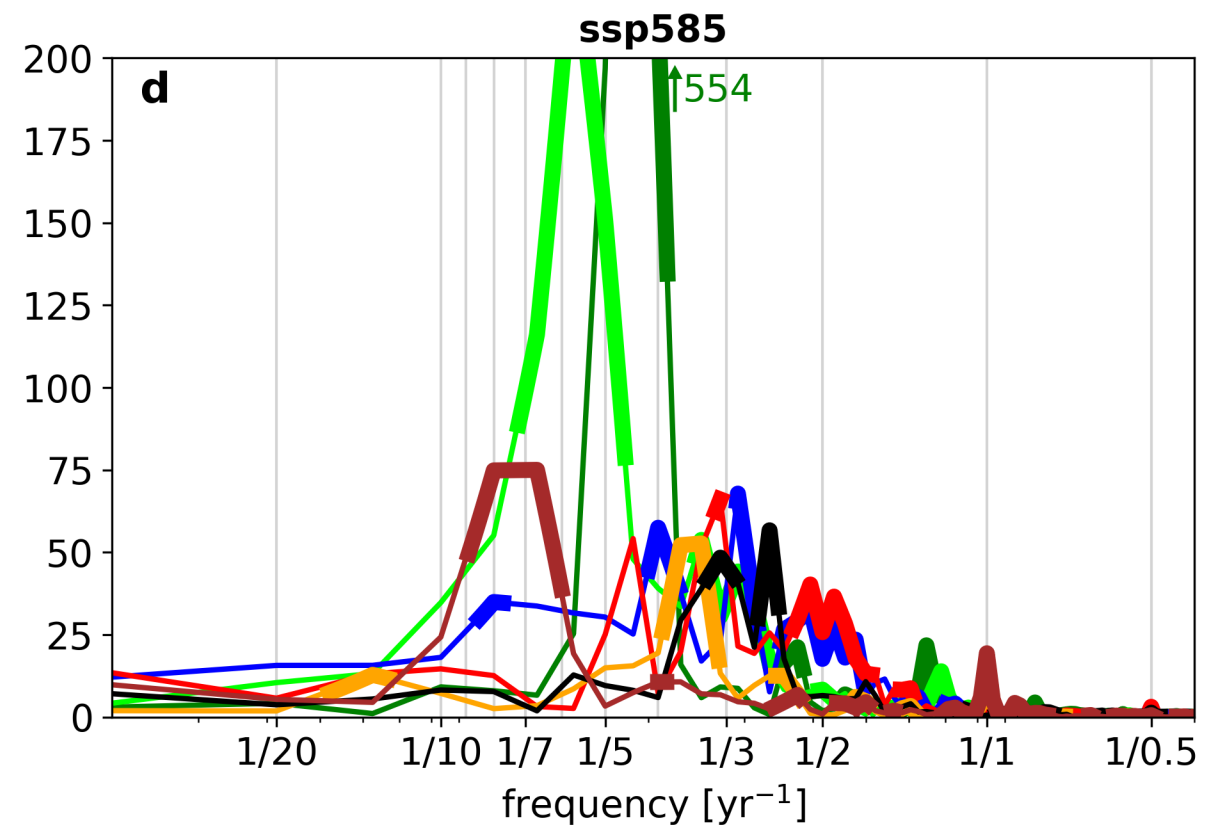
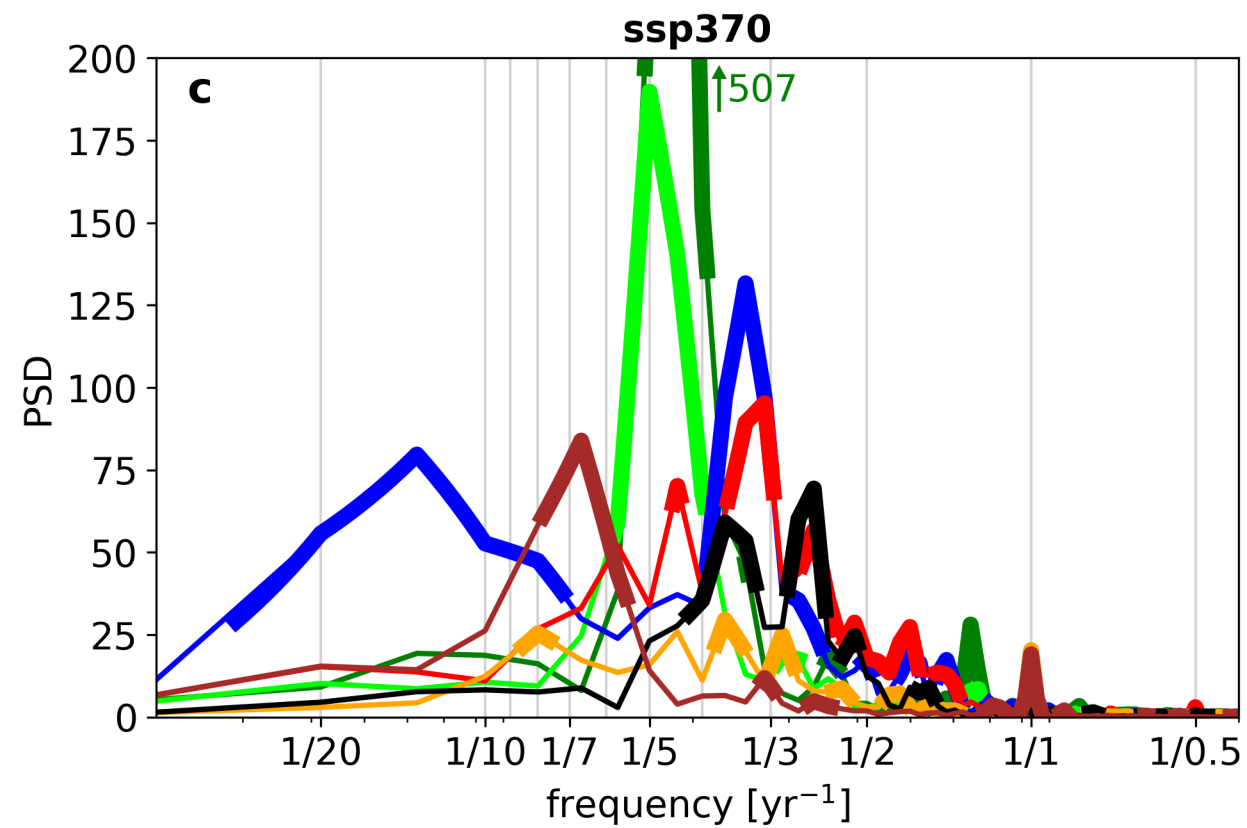
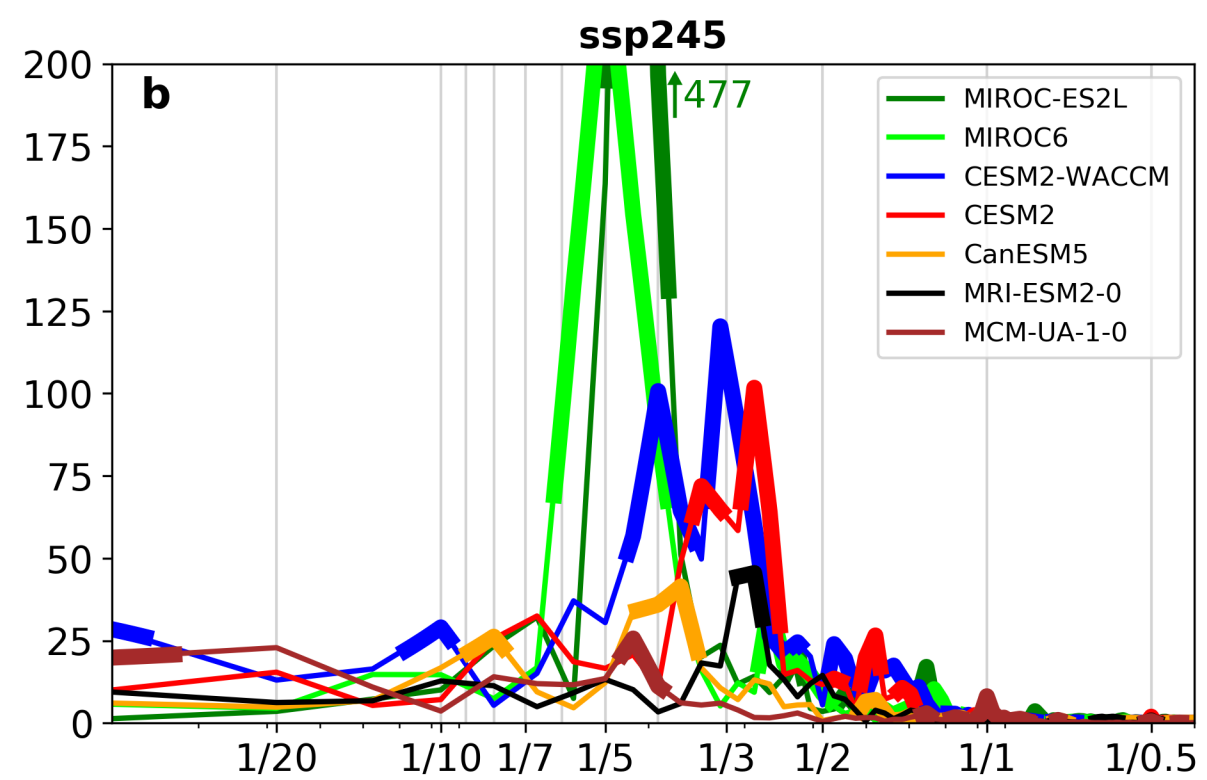
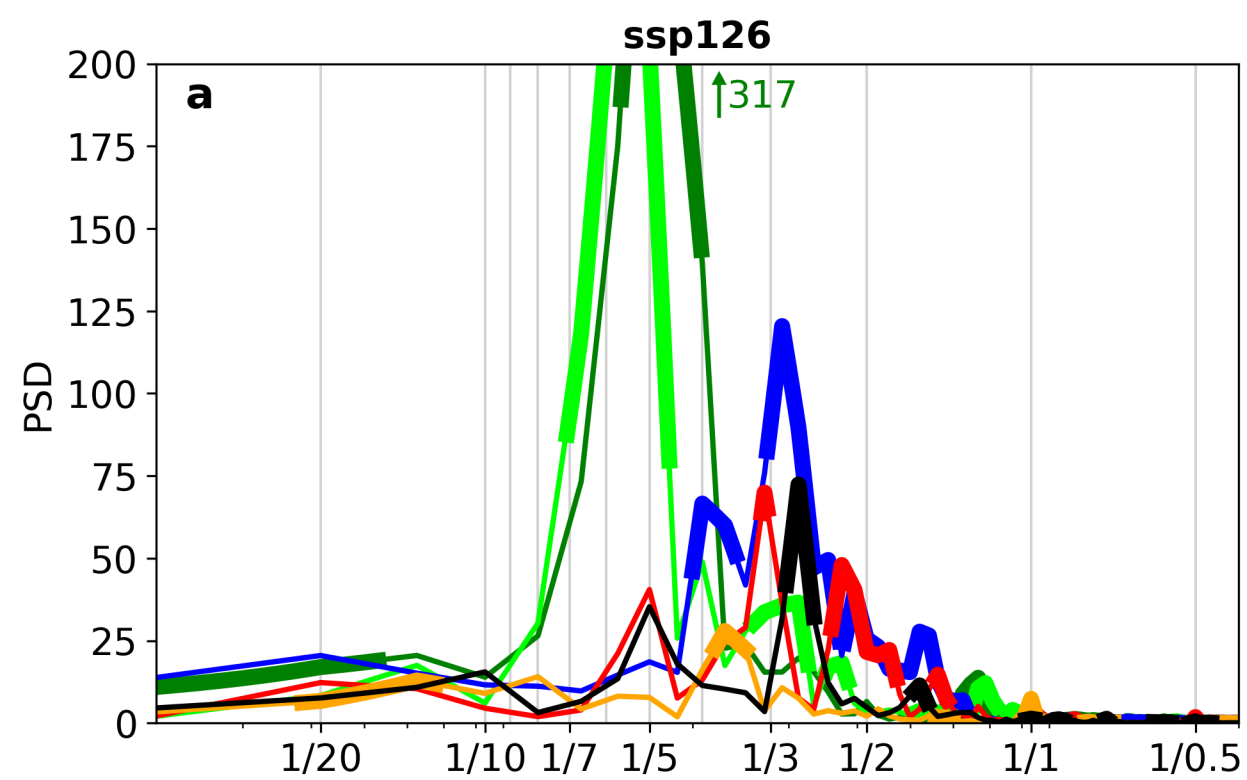


Figure 2.

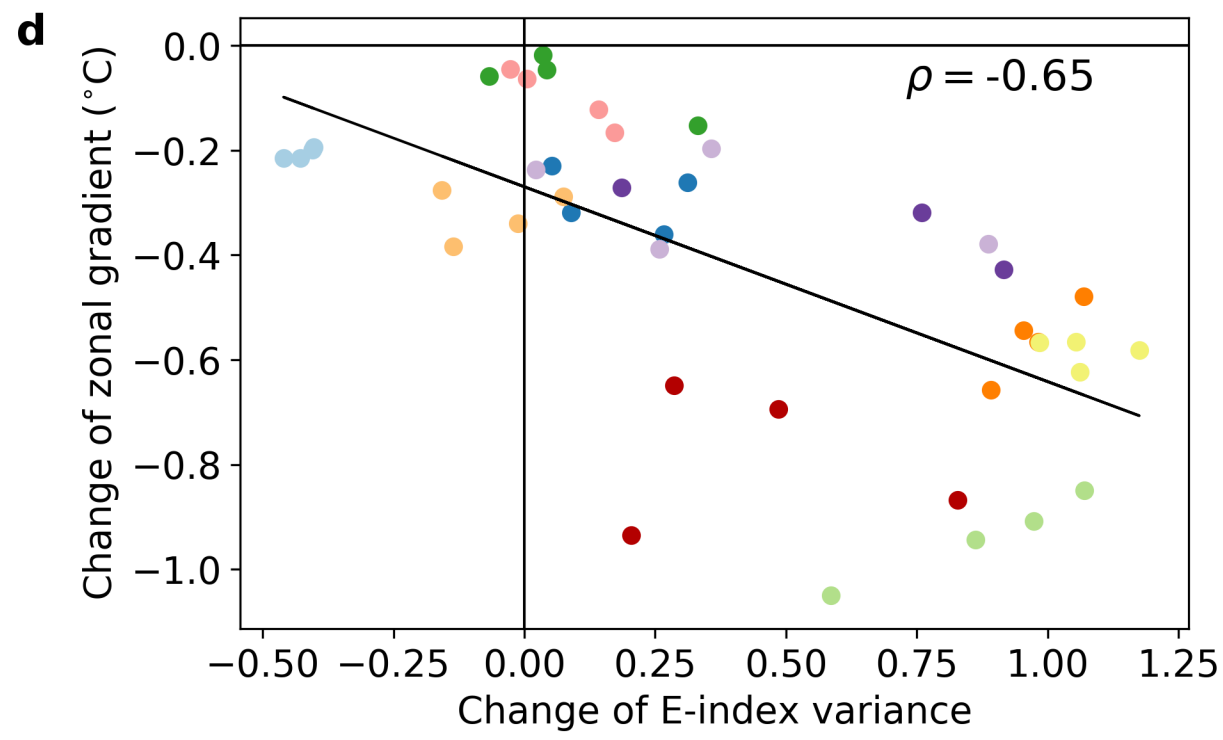
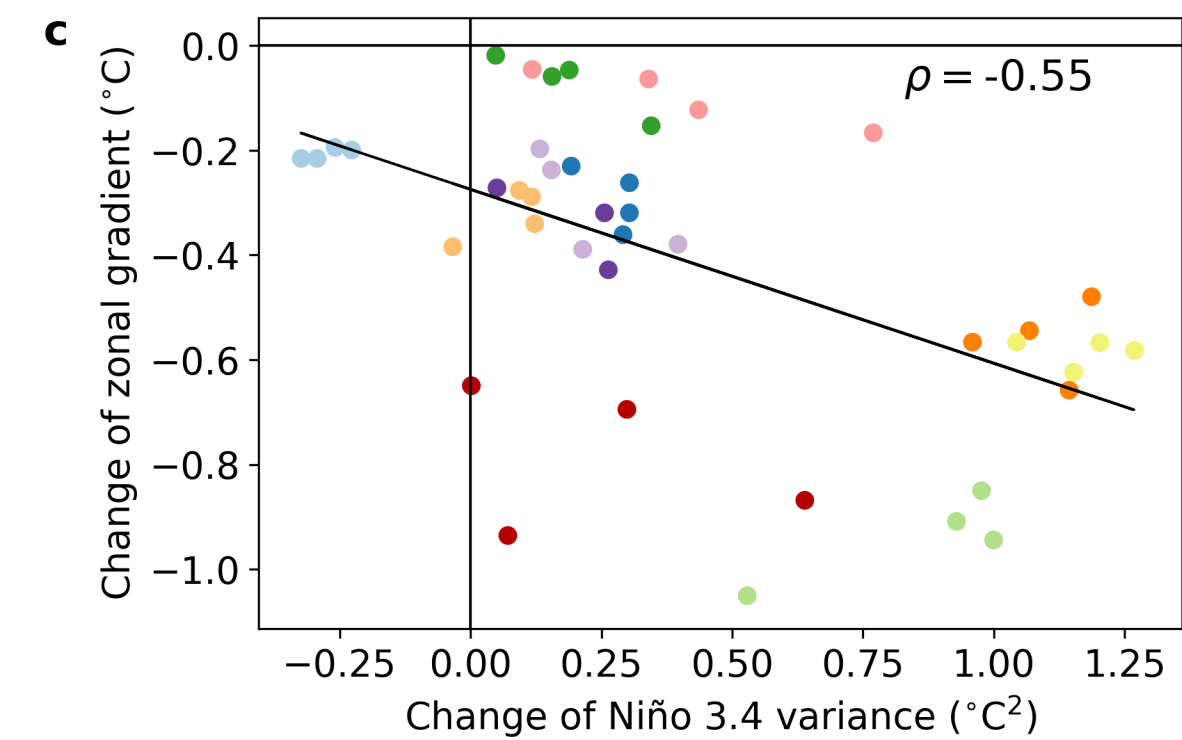
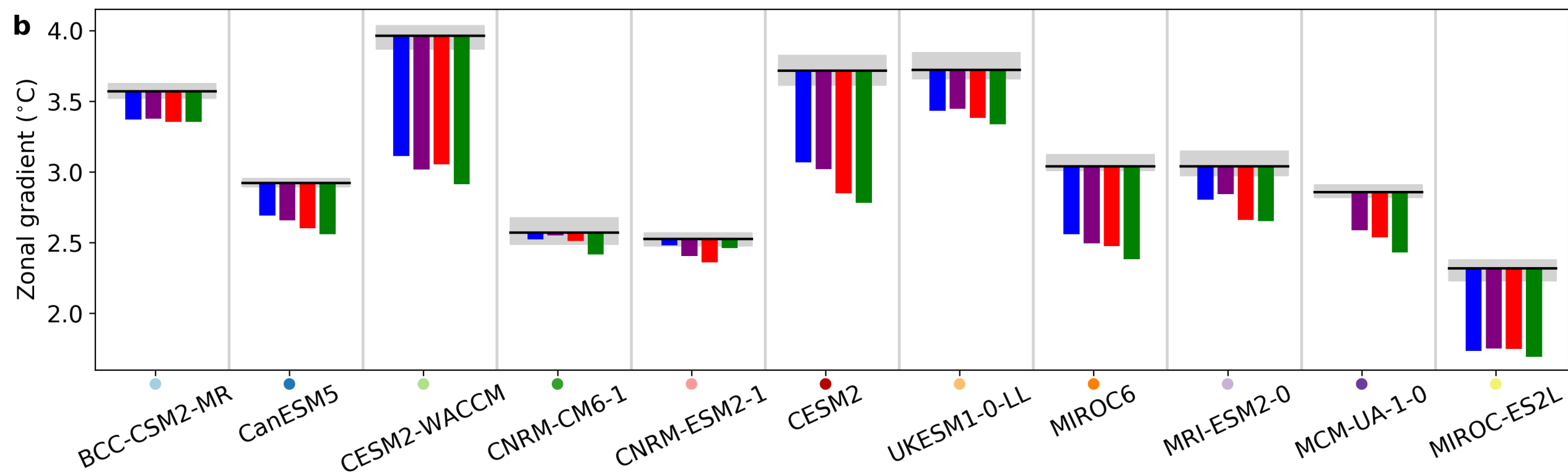
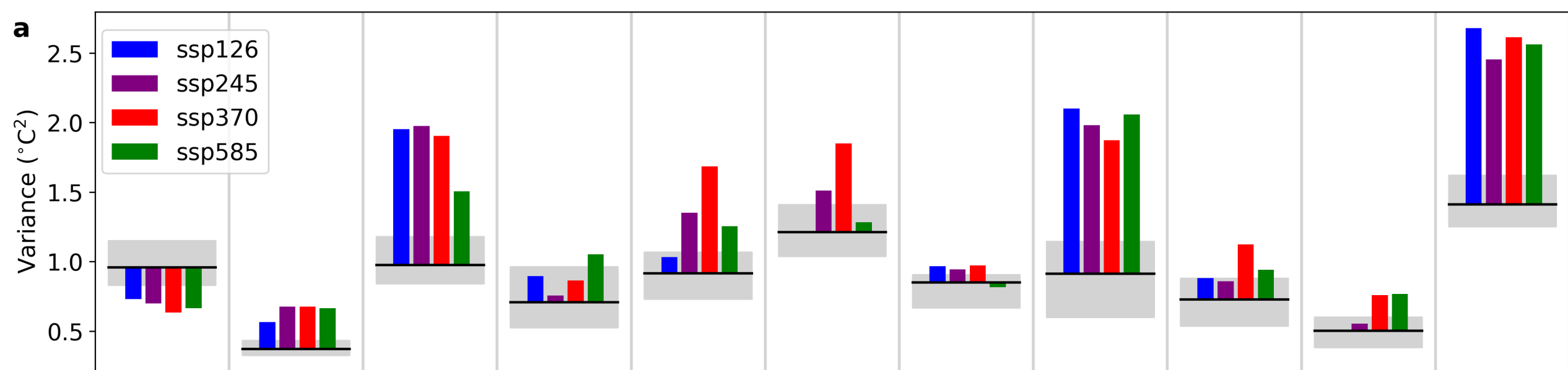


Figure 3.

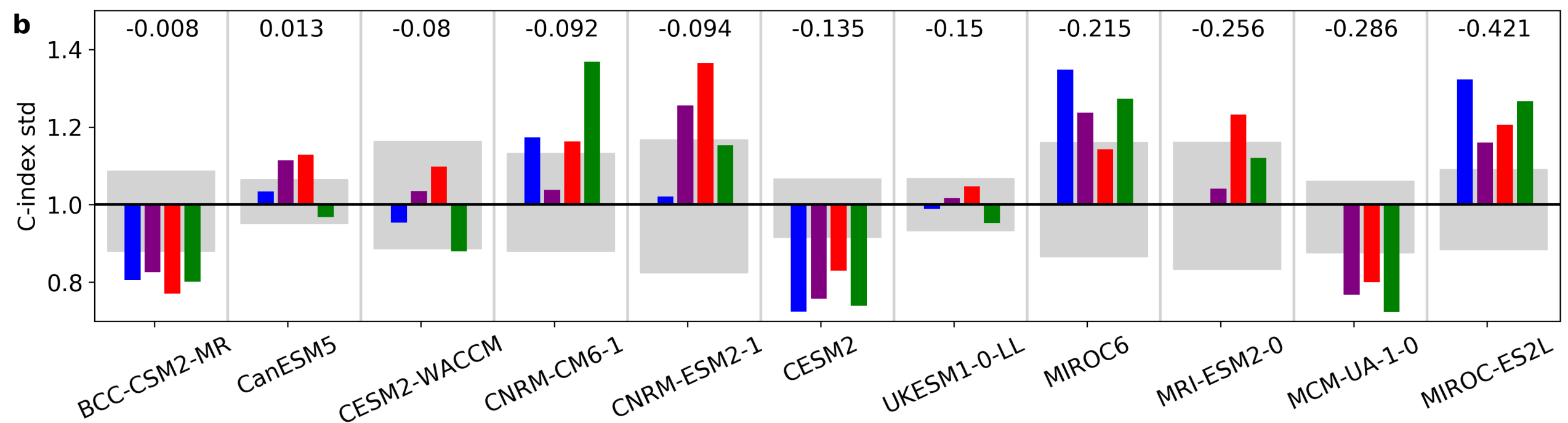
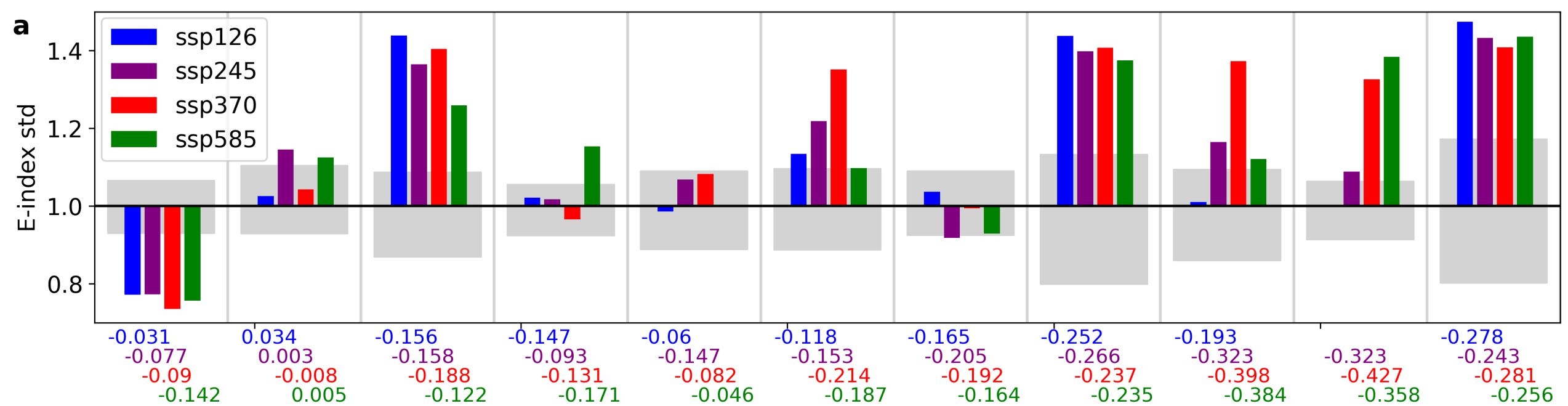
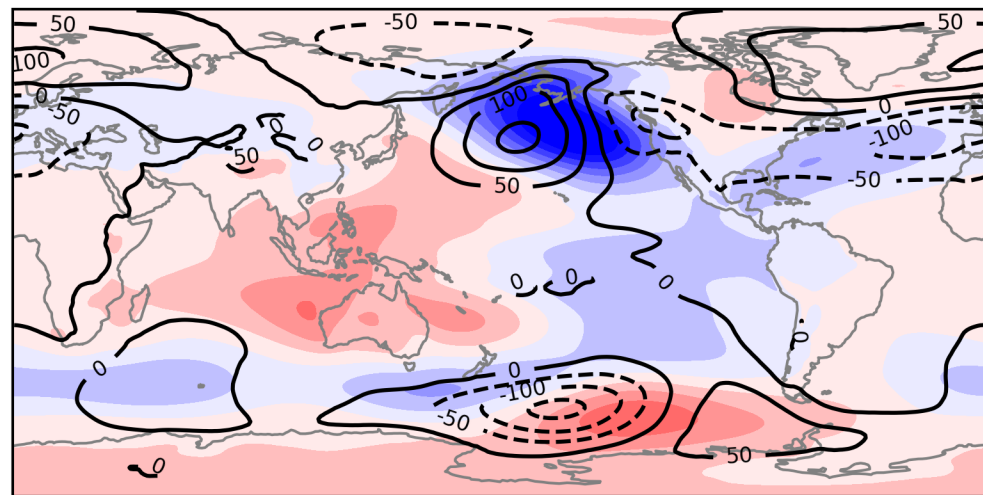
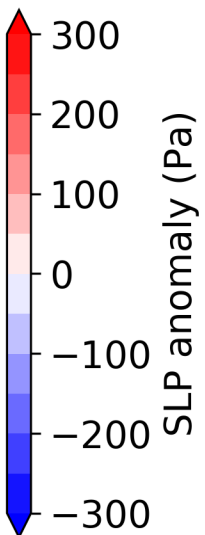
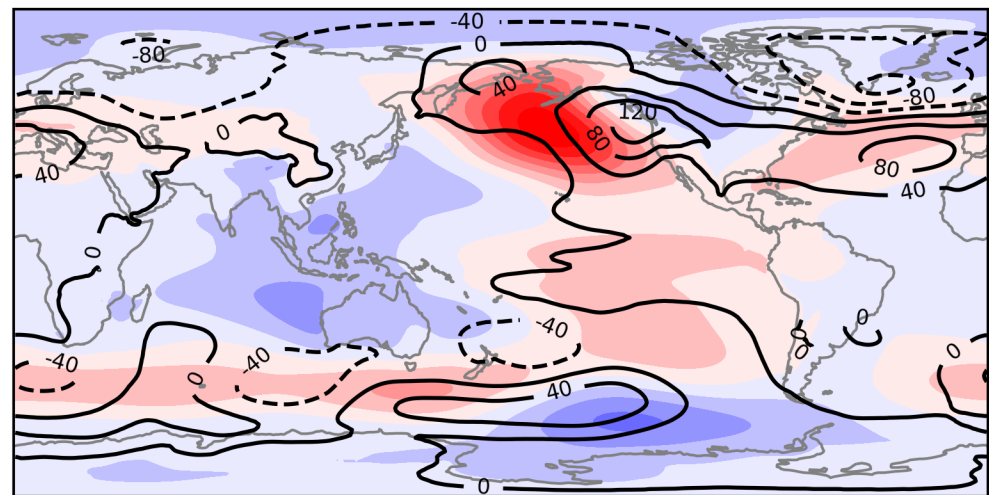


Figure 4.

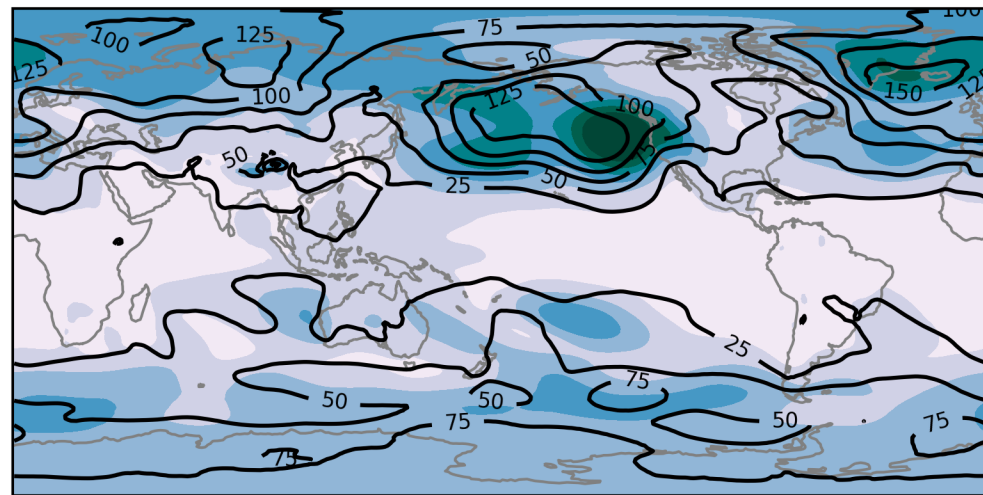
a Model mean El Niño mean sea-level pressure anomaly



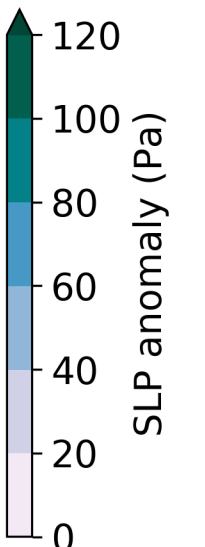
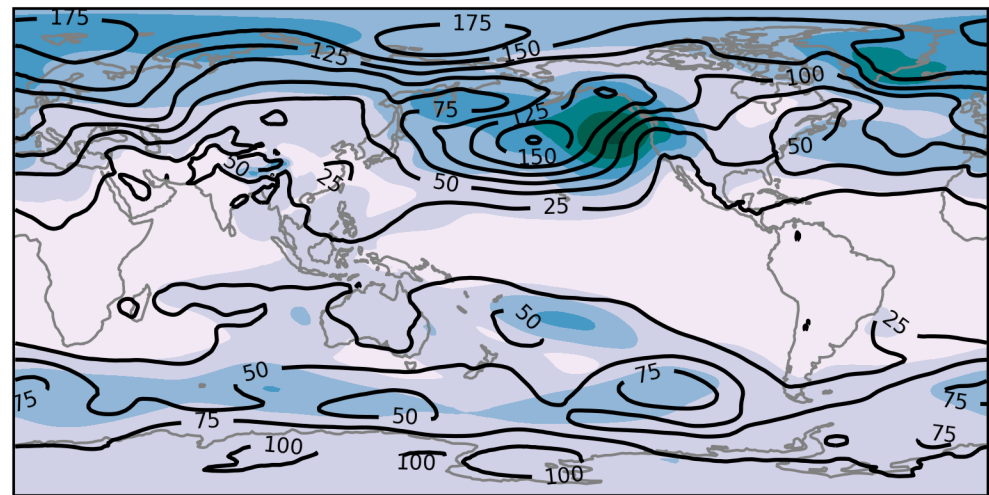
b Model mean La Niña mean sea-level pressure anomaly



c Std of El Niño mean sea-level pressure anomaly



d Std of La Niña mean sea-level pressure anomaly



How does El Niño Southern Oscillation Change Under Global Warming – A First Look at CMIP6

Hege-Beate Fredriksen^{1*}, Judith Berner², Aneesh Subramanian³, Antonietta Capotondi^{4,5}

¹Department of Physics and Technology, UiT the Arctic University of Norway, Tromsø, Norway.

²National Center for Atmospheric Research, Boulder, CO, USA.

³Atmospheric and Oceanic Sciences, University of Colorado Boulder, Boulder, CO, USA.

⁴Cooperative Institute for Research in Environmental Sciences, University of Colorado, Boulder, Colorado, USA.

⁵NOAA Physical Sciences Laboratory, Boulder, CO, USA.

Contents of this file

Text S1 to S3

Figures S1 to S7

Introduction

This supporting information provides further details on the methods and analyses done in the main paper. Text S1 contains an extended description of the data and methods, Text S2 gives a brief discussion of the results of Figure S1, and Text S3 describes some background information for Figures S3 - S6.

Figure S1 shows spectra of the piControl Niño 3.4-index, Figure S2 shows the mean warming of in the Niño 3.4 region for future scenarios, Figures S3 and S4 show patterns associated with the E-index and C-index, Figure S5 shows the quadratic relationship of the two first principal components, Figure S6 the coefficient of the quadratic relationship plotted vs the skewness, and Figure S7 shows teleconnection patterns of sea level pressure for each model.

Text S1: Extended description of data and methods

Data

For the models BCC-CSM2-MR, CanESM5, MIROC6, MRI-ESM2-0, CESM2-WACCM we have used member r1i1p1f1 for all experiments. For models MIROC-ES2L, CNRM-CM6-1, MCM-UA-1-0, UKESM1-0-LL we have used member r1i1p1f2, except for MCM-UA-1-0 piControl, where r1i1p1f1 is used. For this model we note that historical r1i1p1f2 branches from piControl r1i1p1f1. For the model CNRM-ESM2-1 we have used member r1i1p1f2 for piControl, and its child member r2i1p1f2 for historical and future scenarios. For CESM2 we have used r1i1p1f1 for piControl and r4i1p1f1 for the other experiments.

For all piControl simulations, a linear trend is subtracted, to reduce a possible tiny influence of drift. For all future scenarios, a cubic spline detrending is used. When computing the trend, each of the future scenarios are first concatenated with the historical experiment. Then a cubic spline with two internal knots is fitted to the record from 1850 to 2100. The internal knots are chosen to be at the mid year (1932) and end year (2014) of the historical simulation. The only purpose of the historical data in this study is to improve the trend estimates of the future scenarios.

To ensure that the exact same region [5° S - 5° N, 170° W - 120° W] is used for all the models when computing the Niño 3.4-index, models' output is regridded to $1^{\circ} \times 1^{\circ}$ degree resolution prior to spatial averaging. The data have monthly resolution, are smoothed by a 3-month running mean, and piControl mean seasonal variations are subtracted. The variances in Figure 2a and spectral analyses in Figure 1 are computed from anomalies obtained by detrending the Niño 3.4-index.

Spectral analysis

Spectral estimates are computed using Welch overlapped segment averaging on the Niño 3.4 index with monthly resolution. With this method we split the 86-yr long future scenarios into segments of 40 years, with 20 years overlap. For each segment, a windowed periodogram is computed with the Hanning window, then the results of each segment are averaged.

ENSO diversity

Following Cai et al. (2018), EOF analysis is applied to the region 15° S to 15° N, 140° E - 80° W. Before this analysis, models are regridded to a $1^{\circ} \times 1^{\circ}$ grid to ensure the exact same regions are used for all models, then the monthly data are detrended and deseasonalized in each grid point. The first two EOFs and corresponding principal components are computed for piControl, then the two first principal components for future scenarios are estimated by projecting the data onto the piControl EOFs. All principal components are normalized by the estimated standard deviation of the first 500 years of piControl. As Cai et al. (2018) and Takahashi et al. (2011), we compute the E-index as $(PC1 - PC2)/\sqrt{2}$ and C-index as $(PC1 + PC2)/\sqrt{2}$, where the signs of the principal components are defined such that positive PC1 corresponds to positive anomalies in large parts of the Equatorial Pacific, and positive PC2 corresponds to positive anomalies in the western and negative in the eastern part of the Equatorial Pacific. Examples of E and C mode patterns are shown in Supplementary Figure 3.

ENSO teleconnections

An El Niño/La Niña event is defined to occur when the DJF mean exceeds ± 1 standard deviation of the 3-month running mean piControl Niño 3.4-index from the same model. Preprocessing of the sea-level pressures are done as follows for each model: (i) DJF means are computed in all grid points, (ii) detrending in all grid points, (iii) find mean sea-level pressure for all DJF means classified as an El Niño or La Niña event, respectively. The model mean and standard deviations of these results are then computed in Figure 4, after regridding all models to a $1^{\circ} \times 1^{\circ}$ grid.

Text S2: Power spectral density of piControl Niño 3.4-index

Supplementary Figure 1 shows that nine out of eleven models have a piControl spectral peak in the periodicity range 3-7 years. In the high-frequency end we find the model BCC-CSM2-MR, peaking at a period between 2 and 3 years, and in the low-frequency end we find MCM-UA-1-0, peaking at a period of 8 years.

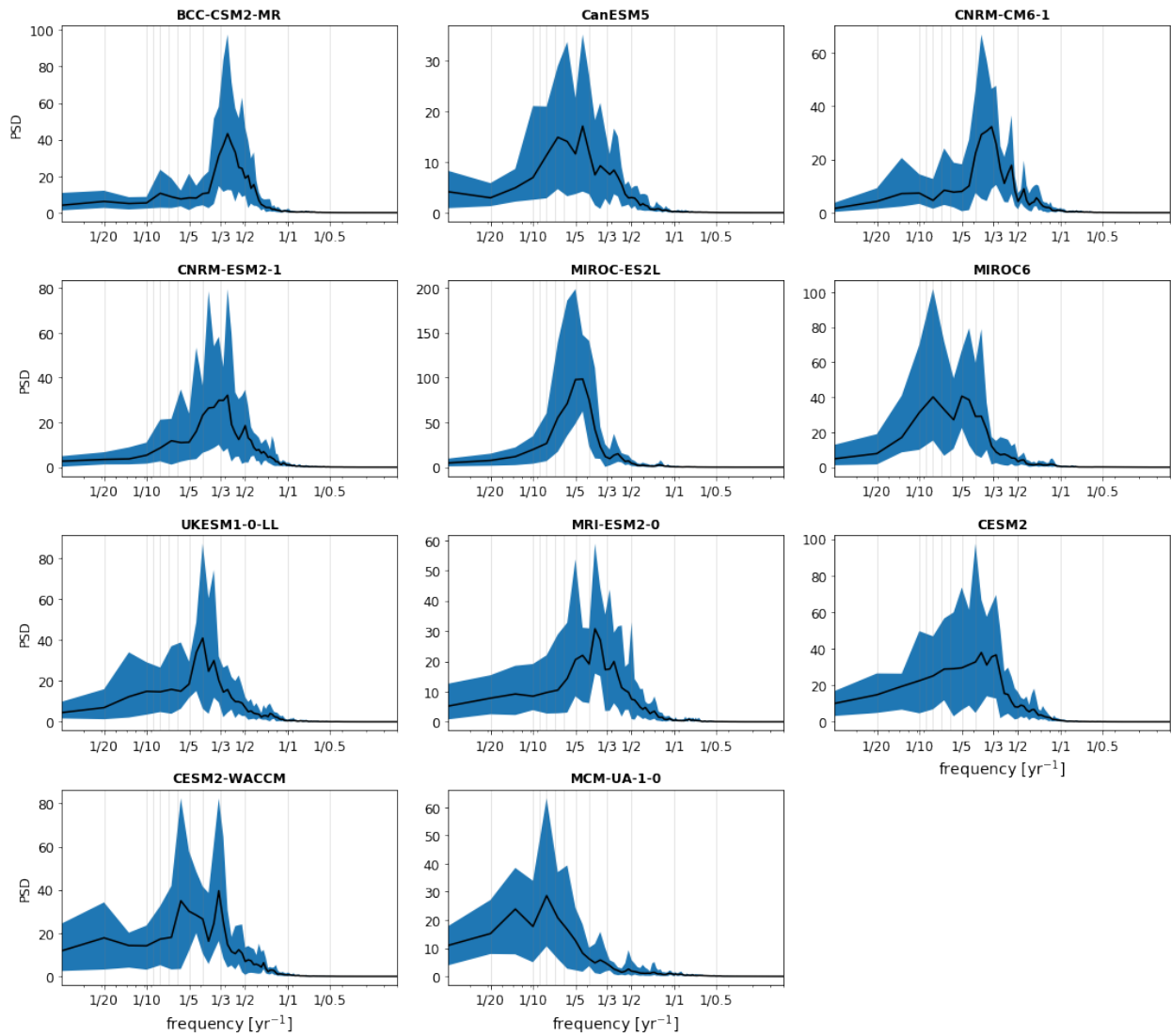


Figure S1. The black curves show the PSDs of the Niño 3.4-index computed using all of the first 500 years of piControl of each of the models. The shaded areas are the spread of the PSDs of 86-yr segments of the control runs, ranging from the minimum to the maximum values.

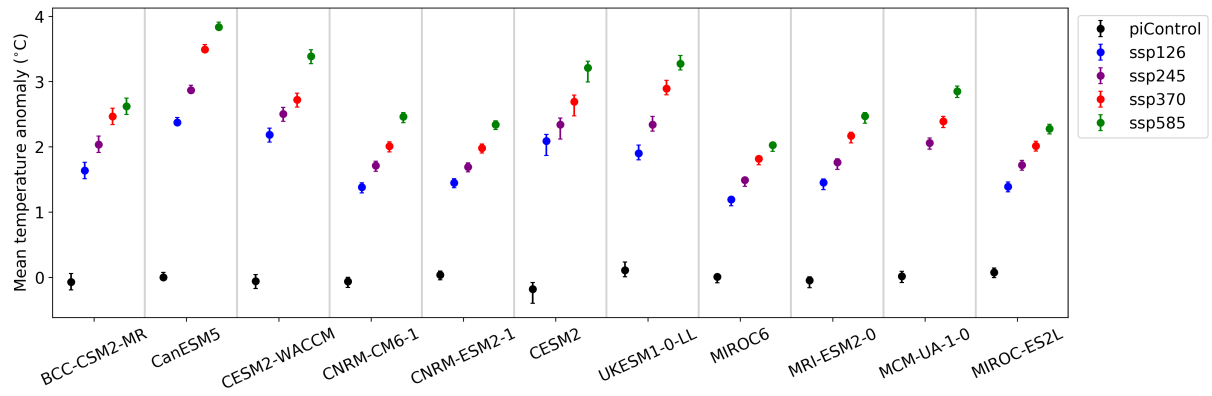


Figure S2: Mean temperature anomaly (°C) in the Niño 3.4 region [5° S - 5° N, 120° W - 170° W] for each of the CMIP6 models for piControl (black), and scenarios ssp126 (blue), ssp245 (purple), ssp370 (red) and ssp585 (green). The anomaly is computed as the difference between the time-averaged absolute temperatures from one member from each experiment and piControl, using monthly data with 3-month running mean. The error bars represent the spread of means in 86-year segments from piControl, ranging from the minimum to the maximum estimates.

Text S3: EP-ENSO and CP-ENSO patterns

The patterns associated with EP-ENSO and CP-ENSO are here calculated following the definition of Takahashi et al. (2011) as:

$$EP - ENSO \text{ pattern} = \frac{\sqrt{2}}{2}(EOF1 \cdot std(PC1) - EOF2 \cdot std(PC2)) \quad (1)$$

$$CP - ENSO \text{ pattern} = \frac{\sqrt{2}}{2}(EOF1 \cdot std(PC1) + EOF2 \cdot std(PC2)) \quad (2)$$

These expressions are derived such that:

$$\begin{aligned} PC1(t) \cdot EOF1 + PC2(t) \cdot EOF2 \\ = C - index(t) \cdot CP - ENSO \text{ pattern} + E - index(t) \cdot EP - ENSO \text{ pattern} \end{aligned}$$

The patterns obtained using this method are very similar to patterns obtained by performing a regression of the fields onto the C-index and E-index. The patterns for CESM2 are shown in Figure S3, and for the other models in Figure S4.

Following Karamperidou et al. (2017) and Cai et al. (2018), we estimate parameters in a quadratic relationship between PC1 and PC2:

$$PC2 = \alpha PC1^2 + \beta PC1 + \gamma$$

The scatterplots of PC1-PC2, as well as the estimated values of α are shown in Figure S5, while the relationships between α and the skewness of the E and C indices (Cai et al., 2018) are displayed in Figure S6.

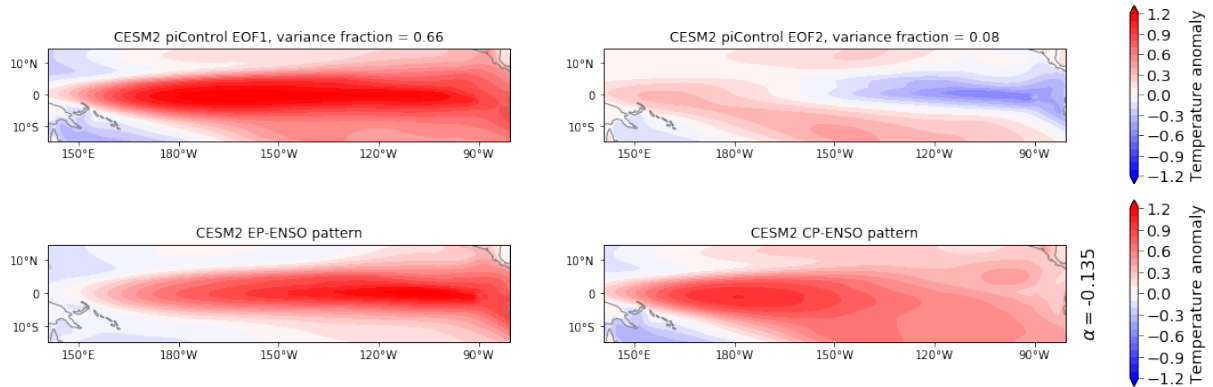


Figure S3: EOF1 and EOF2 for CESM2 (top row), and patterns associated with CP-ENSO and EP-ENSO (bottom row), calculated using Eqs. (1), (2). The patterns are scaled such that their corresponding principal component or index have standard deviation 1.

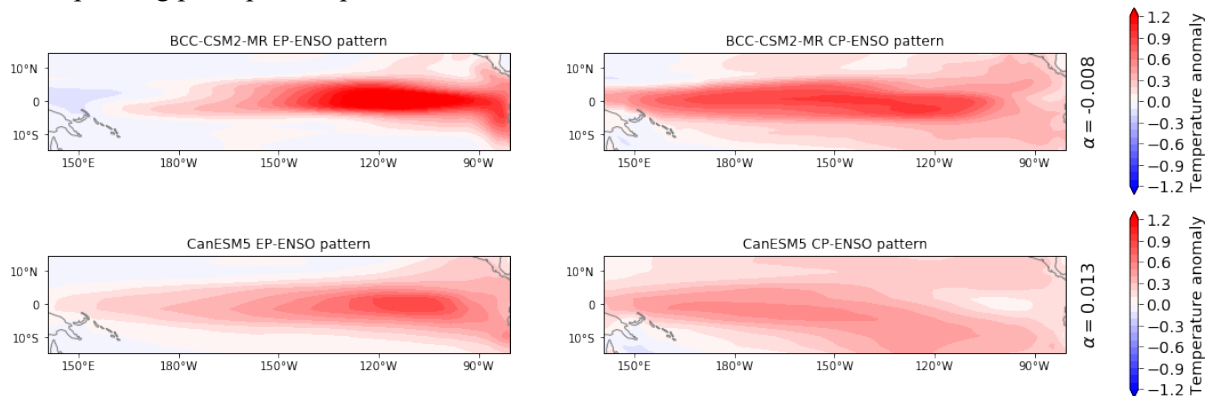


Figure S4: Patterns associated with CP-ENSO and EP-ENSO calculated using Eqs. (1), (2). The patterns are scaled such that their corresponding index have standard deviation 1.

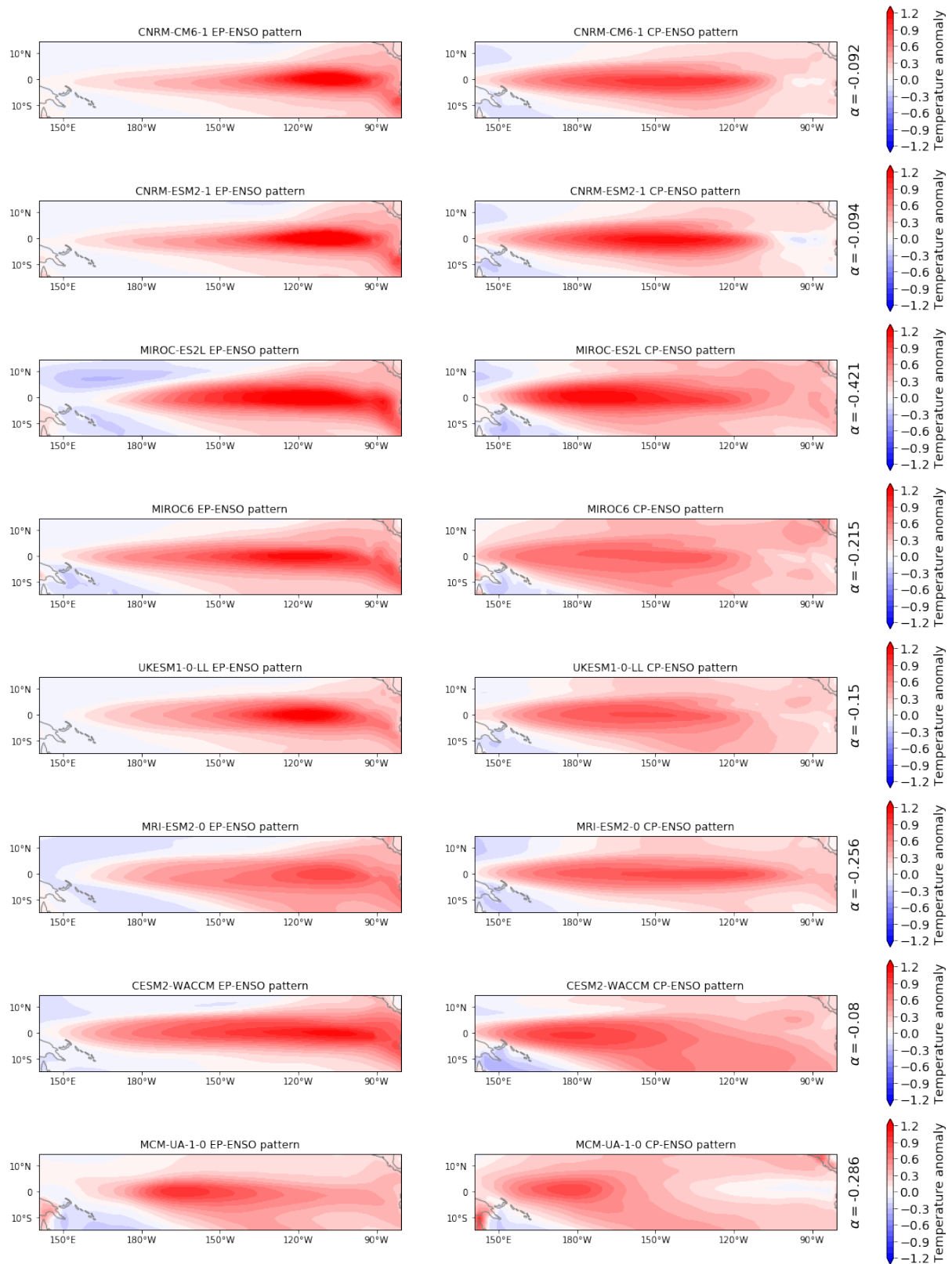


Figure S4 continued.

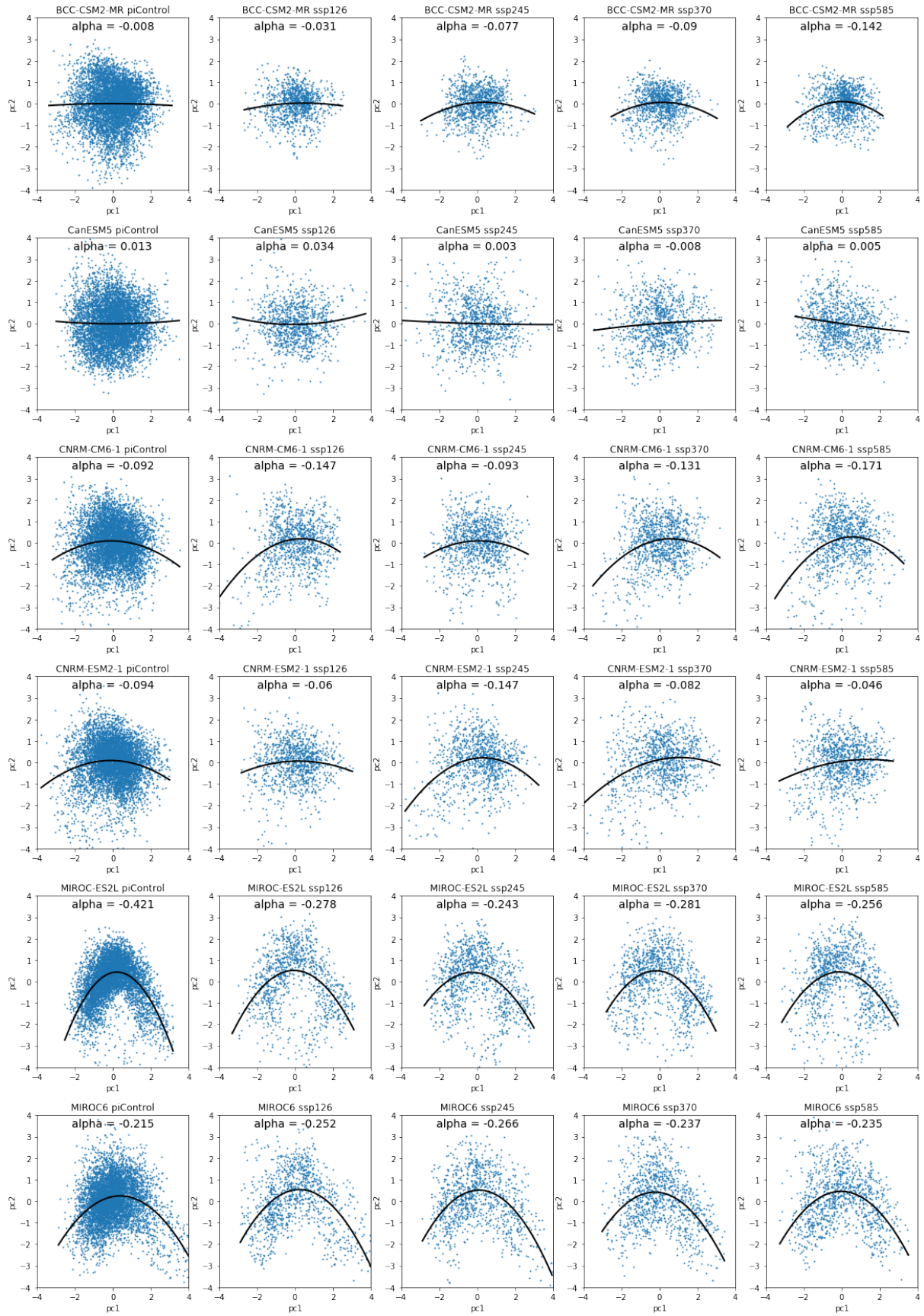


Figure S5: Scatterplots of PC1 vs PC2 for all models and scenarios in this study, and quadratic fits (black curves).

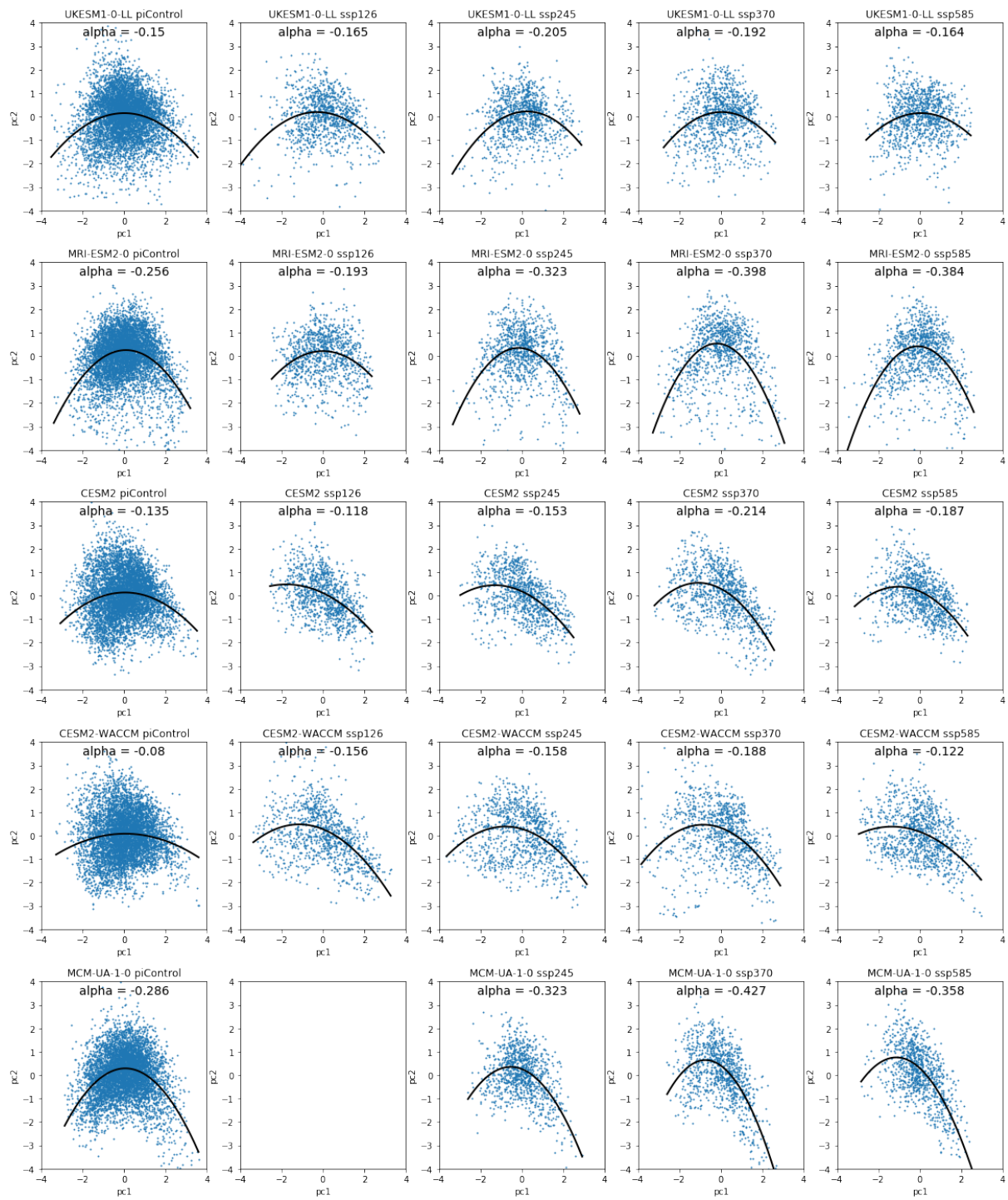


Figure S5 continued.

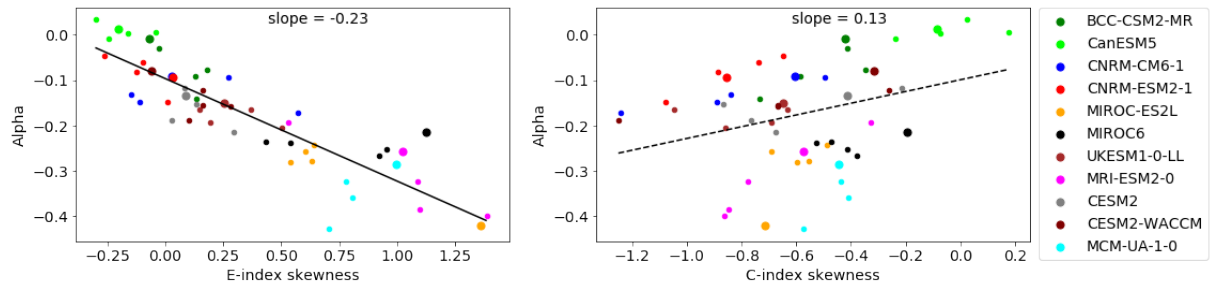


Figure S6: Estimates of alpha vs skewness of E-index and C-index. The five estimates for each model represent different experiments: large circles are from piControl, and used to sort models in main Figure 3, and the smaller circles are from SSP scenarios.

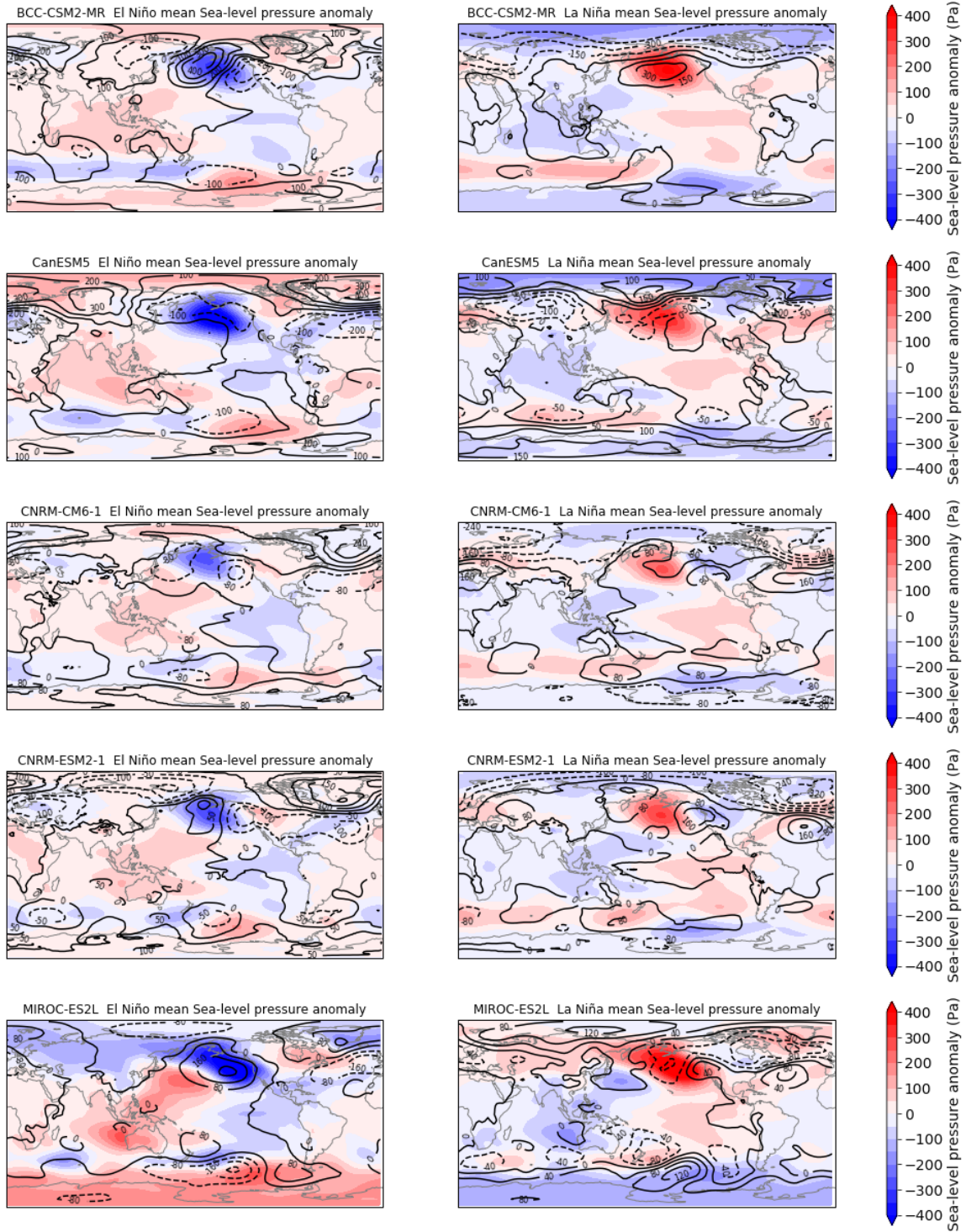


Figure S7: Showing the same as main Figure 4 a) and b), but for each model.

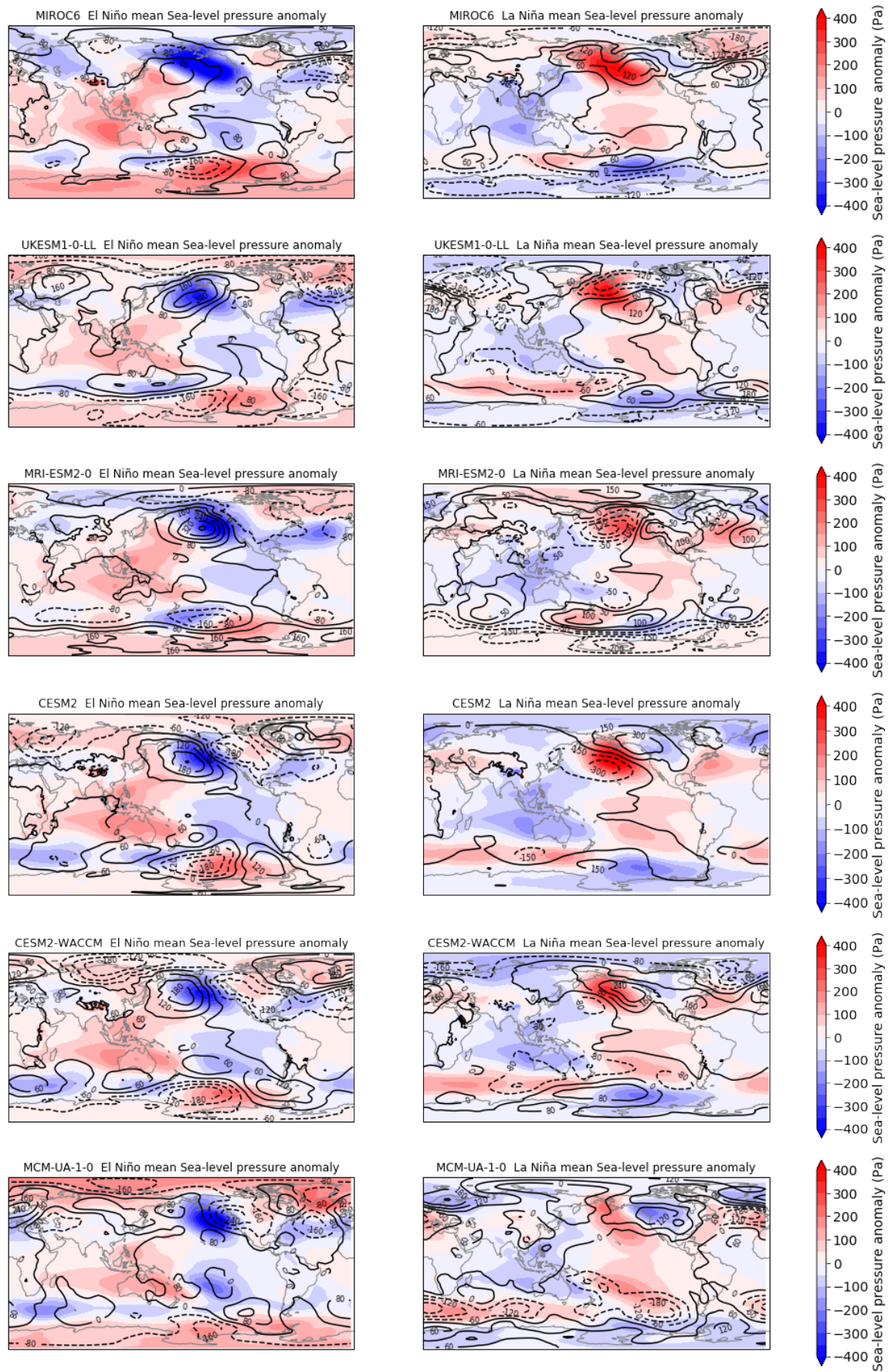


Figure S7 continued.